# Evaluating land surface phenology from the Advanced Himawari Imager using observations from MODIS and the Phenological Eyes Network

**Dong Yan[1*], Xiaoyang Zhang[1, 2], Shin Nagai[3], Yunyue Yu[4], Tomoko Akitsu[5], Kenlo Nishida Nasahara[5], Reiko Ide[6], Takahisa Maeda[7]**

[1]Geospatial Sciences Center of Excellence, South Dakota State University, 1021 Medary Ave, Wecota Hall 115, Box 506B, Brookings, SD 57007, USA.

[2]Department of Geography, South Dakota State University, 1021 Medary Ave, Wecota Hall 115, Box 506B, Brookings, SD 57007, USA.

[3]Research and Development Center for Global Change, Japan Agency for Marine-Earth Science and Technology, 3173-25 Showa-machi, Kanazawa-ku, Yokohama 236-0001, Japan.

[4]NOAA/NESDIS/STAR, 5200 Auth Rd, Camp Springs, MD 20746, USA.

[5]Faculty of Life and Environmental Sciences, University of Tsukuba, 1-1-1, Tennoudai, Tsukuba, Ibaraki, 305-8572, Japan.

[6]Center for Global Environmental Research, National Institute for Environmental Studies, Onogawa 16-2, Tsukuba 305-8506, Japan.

[7]Environmental Management Research Institute, National Institute of Advanced Industrial Science and Technology (AIST) AIST Tsukuba West, Onogawa 16-1, Tsukuba 305-8569, Japan.

* Corresponding author: Dong Yan (yand@email.arizona.edu)

Present address: 1064 E Lowell St., Tucson, AZ 85719, USA.

## Abstract

The Advanced Himawari Imager (AHI) onboard the recently launched next generation geostationary satellite, Himawari-8, provides an opportunity to improve Land Surface Phenology (LSP) detections over the Asia-Pacific region. In this paper, we detected four phenological transition dates (PTDs) using the three-day Two-band Enhanced Vegetation Index (EVI2) time series from AHI based on the Hybrid Piecewise Logistic Model-Land Surface Phenology Detection (HPLM-LSPD) algorithm. The four PTDs are Start of Spring (SOS), End of Spring (EOS), Start of Fall (SOF) and End of Fall (SOF). We evaluated the four AHI-derived PTDs against those detected using eight-day EVI2 time series from the Moderate Resolution Imaging Spectroradiometer (MODIS) onboard the polar-orbiting satellite Terra, and three-day Green Chromatic Coordinate (GCC) time series from the Phenological Eyes Network (PEN) at six sites in central and northern Japan. The evaluation was performed by conducting regression analyses, and calculating root mean square difference (RMSD) and bias between satellite- and PEN-derived PTDs. First, the difference in the spatial variations of SOS and EOF timing between naturally vegetated areas, and urban areas and croplands indicates the anthropogenic footprints on LSP. Second, the RMSD of either AHI PTDs or MODIS PTDs against PEN PTDs were higher in the fall (i.e., SOF and EOF) than those in spring (i.e., SOS and EOS). Third, the later EOS and earlier SOF derived from satellite EVI2 relative to those derived from PEN GCC might be caused by the difference in the sensitivity of GCC and EVI2 to the increases in leaf area index (LAI) over high-LAI canopies. Fourth, the higher temporal resolution of AHI EVI2 only helped reduce the RMSD during spring compared to the RMSD for MODIS. In contrast, the RMSD for AHI PTDs and MODIS PTDs were comparable in fall. Finally, the between-sensor correlation in the spatiotemporal variability of the four PTDs was higher for SOS and EOF than those for EOS and SOF.



**Key words**: Geostationary satellites, AHI, MODIS, Land surface phenology, Phenological Eyes Network.


## 1. Introduction

Land surface phenology (LSP) refers to the seasonal changes in remotely sensed greenness over vegetated land surfaces (de Beurs & Henebry 2005). LSP exerts a strong control over many important ecosystem processes such as carbon, water and nutrients cycling (Richardson et al. 2013), and is a sensitive indicator of both climatic and anthropogenic changes (Zhang et al. 2004b; de Beurs & Henebry 2008; Richardson et al. 2013). Therefore, LSP has been widely detected from polar-orbiting satellites such as the Advanced Very High Resolution Radiometer (AVHRR) and the Moderate Resolution Imaging Spectroradiometer (MODIS), at regional and global scales based on the seasonal dynamics of greenness indices such as Normalized Difference Vegetation Index (NDVI) and Enhanced vegetation index (EVI) (de Beurs & Henebry 2005; Ganguly et al. 2010; Zhang et al. 2018a). Although polar-orbiting satellites are able to provide daily observations with global coverage, frequent cloudy conditions can obstruct the accurate characterizations of LSP, particularly in cloud-prone regions (Zhang et al. 2006, 2017; Fensholt et al. 2007). For example, less than 10% of AVHRR observations over North America were cloud-free for any given month during 1982-2016 (Zhang, 2015), and MODIS observations in more than 27% of the Earth's land surface could be consecutively affected by clouds for more than 16 days during vegetation growing seasons (Zhang et al., 2006). Prolonged cloudy conditions during vegetation growing seasons could significantly reduce the accuracy of LSP detections (Zhang et al., 2009).

Geostationary satellites offer sub-hourly observations, which allow much higher chances to obtain cloud-free observations (Fensholt et al. 2007; Guan et al. 2014; Yan et al. 2016a). The advantage of geostationary satellites has been demonstrated by comparing the data quality of NDVI composites between MODIS and the geostationary Spinning Enhanced Visible and Infrared Imager (SEVIRI) during the rainy season across the cloud-prone West Africa (Fensholt et al., 2007). The results show that cloud-free SEVIRI NDVI composites throughout the 2004 growing season accounted for 87% of the pixels in West Africa while cloudy MODIS NDVI composites occurred at least once in 96% of the pixels in the same region. Further, the LSP detections from SEVIRI and MODIS data were also inter-compared over the cloud-prone Congo Basin (Yan et al., 2016) and results show that SEVIRI is able to reveal more widespread seasonality of tropical rainforests than MODIS does. Currently, only a handful of studies have investigated LSP detections from geostationary satellites and compared them with LSP detections from polar-orbiting satellites (Sobrino et al. 2013; Guan et al. 2014; Yan et al. 2016a). However, such studies were only conducted in Africa while the performance of LSP detections from geostationary satellites is unknown in other continents. Moreover, there is a lack of quantitative comparisons between LSP detected using observations from geostationary and polar-orbiting satellites with ground-based observations as an independent reference.

Evaluating the uncertainties in LSP detections is challenging because LSP is different from ground-based phenological observation in scale. Previous studies on LSP evaluations have mainly used *in situ* phenological observations (Zhang et al. 2006; Soudani et al. 2008; Ganguly et al. 2010; Liang et al. 2011; Klosterman et al. 2014; Delbart et al. 2015; Rodriguez-Galiano et al. 2015) and gross primary productivity measured using the eddy covariance technique (Sakamoto et al. 2010; Gonsamo et al. 2012; Lu et al. 2018). However, the reference data used in these assessments are not intrinsically comparable with satellite-derived LSP. The emergence of observation networks, such as the Phenological Eyes Network (PEN) (http://www.pheno-eye.org/) and the PhenoCam Network (https://phenocam.sr.unh.edu/webcam/) that employ tower-mounted camera to automatically collect time-lapse photography, greatly enriches the availability of ground-based phenological observations (Nasahara & Nagai 2015; Brown et al. 2016; Nagai et al. 2016b, 2018; Richardson et al. 2018a). These observations have been shown to be a robust tool to evaluate the LSP derived from satellite remote sensing (Klosterman et al. 2014; Richardson et al. 2018b). The PhenoCam Network mainly provides observations in the United States (Richardson et al., 2009a), while PEN mainly covers Japan with the recent extension to the Arctic and the Tropics (Nagai et al. 2018). The PEN was established in 2003 to provide long-term, continuous, and consistent ground-based phenological observations (Nasahara & Nagai 2015; Nagai et al. 2016b). It employs cameras mounted at different positions to provide a comprehensive picture of phenological changes in the ecosystem (Nagai et al. 2018). The time-lapse images collected by PEN have been used in a wide range of scientific studies including: 1) exploring the phenological changes at ground level in understudied ecosystems such as evergreen forests and tropical rainforests (Nagai et al. 2013, 2016a; Kobayashi et al. 2018), 2) evaluating the quality of satellite-derived LSP (Motohka et al. 2009), and 3) modeling ecosystem productivity (Nagai et al. 2010).

The recently launched next generation geostationary satellite, Himawari-8, provides an opportunity to quantitatively evaluate LSP detections from geostationary satellites in the Asia-Pacific region. This study presents the results from the first attempt to detect the phenological transition dates from the Advanced Himawari Imager (AHI) onboard the Himawari-8 geostationary satellite over central and northern Japan, and the evaluation results of the detected phenological transition dates. The evaluation was performed by comparing the detected phenological transition dates from AHI against those detected from MODIS and PEN at six selected sites during 2015 and 2016.

## 2. Methods

### **2.1** AHI EVI2 time series

Himawari-8 was launched on October 7, 2014 and is positioned over the Equator at 140.7°E (Yu and Wu 2016). The AHI onboard Himawari-8 delivers a full disk scan covering the Asia-Pacific region every ten minutes with a nadir resolution of 500 – 1000m in the visible/near-infrared spectrum (Yu and Wu 2016). We obtained the spectral radiance of AHI band 3 (0.64 µm, nadir resolution 500 m) and band 4 (0.86 µm, nadir resolution 1000 m) at a 20-minute interval during Tokyo local time 8:00am-4:00pm from May, 2015 to November, 2016 with a spatial coverage of central and northern Japan from the HimawariCloud dissemination service (Yu and Wu 2016). The band 3 radiance data were first resampled to match those of band 4 spatially. The radiance data were then converted to Top-of-Atmosphere (TOA) reflectance for calculating 20-minute EVI2 when solar zenith angle was less than 60° (Yan et al. 2016a; Yan et al. 2016b). Similar to EVI, EVI2 has the capability of reducing background noise and has enhanced sensitivity over dense vegetation canopies. In addition, EVI2 has been shown to have advantages over commonly used NDVI in LSP detections (Peng et al. 2017; Zhang et al. 2018b) and EVI2 has been widely used for LSP detections across a wide range of ecosystems globally (Liu et al. 2017; Yan et al. 2016a; Yan et al. 2016b; Zhang 2015; Zhang et al. 2017). EVI2 was calculated using equation (1)(Jiang et al. 2008):

$$EVI2 = G\frac{NIR - R}{NIR + cR + 1} \tag{1}$$

where NIR and R refer to the reflectance from AHI band 4 and band 3, respectively. EVI2 is originally developed for MODIS with G and c being 2.5 and 2.4 in equation (1), respectively. The original values of G and c have been adopted to calculate EVI2 from other sensors such as AVHRR (Zhang 2015) and the Visible Infrared Imaging Radiometer Suite (VIIRS) (Zhang et al. 2018a) for LSP monitoring. LSP generated using the EVI2 from AVHRR and VIIRS has been shown to have strong agreements with those derived from independent sources such as eddy covariance measurements (Zhang 2015) and PhenoCam Imagery (Zhang et al. 2018a). We therefore believe it is appropriate for us to use the original values of G (2.5) and c (2.4) in this study.

The angular effects in AHI EVI2 were further minimized. To do this, each 20-minute EVI2 was converted to an EVI2 obtained under a reference sun-satellite geometry using equation (2) (Tian et al. 2010):

$$EVI2(\theta_{REF}, \delta_{REF}, \phi_{REF}) = EVI2(\theta_t, \delta_t, \phi_t)\frac{(1+C_0FS_{REF}+C_1FR_{REF})}{(1+C_0FS_t+C_1FR_t)} \tag{2}$$

where $EVI2(\theta_{REF}, \delta_{REF}, \phi_{REF})$ is the angularly-corrected EVI2 under the reference sun-satellite geometry ($\theta_{REF} = 45°, \delta_{REF} = 45°, \phi_{REF} = 90°$); $\theta$ is the solar zenith angle, $\delta$ is the satellite zenith angle; $\emptyset$ is the sun-satellite relative azimuth angle; $EVI2(\theta_t, \delta_t, \phi_t)$is the original EVI2 obtained under the sun-satellite geometry $(\theta_t, \delta_t, \phi_t)$ at time $t$; $FS$ and $FR$ represent the kernel functions that model the variations in EVI2 due to changes in sun-satellite geometry. $C_0$ and $C_1$ are kernel weights that were determined as -0.08 and 0.02, respectively, for AHI EVI2 based on the method proposed in a previous study (Tian et al. 2010). Finally, a 3-day EVI2 time series was obtained by calculating the 90$^{th}$ percentile of all the 20-minute angularly-corrected EVI2 within each 3-day period during 2015-2016. Since AHI pixel size varies with the view zenith angle, we resampled EVI2 time series to 0.02° (~2000m) grid cells using a nearest neighbor method.

**2.2** MODIS EVI2 time series

To compare with AHI LSP detections, we also generated EVI2 time series using the 8-day 500m MODIS surface reflectance product (MOD09A1) downloaded using the MODIS Land Products Global Subsetting and Visualization Tool (ORNL-DAAC 2018). The MODIS EVI2 time series was only generated at six selected PEN sites in Japan, locations and land cover of which are described in detail in Section 2.4. Specifically, we first calculated EVI2 for each 500m pixel within a five-by-five pixel window centering at a given PEN site. Then for each 8-day period, we aggregated EVI2 by averaging EVI2 values from pixels with good quality within the five-by-five pixel window (based on the quality assurance data in the MOD09A1 product). A fill value was used if good quality pixels were less than half of the pixels within the window. Thus, the MODIS EVI2 was spatially comparable to AHI EVI2.

### **2.3** Land surface temperature and snow cover time series from MODIS observations

Satellite observations can be affected by snow during winter in mid- and high- latitude regions, which has significant impacts on LSP detections (Zhang et al., 2004). To determine winter period and remove snow-affected observations, we obtained land surface temperature (LST) and snow presence data in Japan during 2015-2016. Specifically, we downloaded the 8-day 1km MODIS land surface temperature (LST) product (MOD11A2) from NASA Earthdata (https://earthdata.nasa.gov/) and the MODIS 8-day 500m snow cover product (MOD10A2) derived from the Normalized Difference Snow Index from the National Snow and Ice Data Center (https://nsidc.org/data/mod10a2) (Riggs et al. 1994). The MODIS LST and snow data were resampled to a spatial resolution of 0.02° to match that of AHI EVI2. Further, a 3-day LST and snow time series were generated based on the interpolation method developed in Zhang (2015) to match the temporal resolution of the AHI EVI2 time series.

### **2.4** Green chromatic coordinate time series from the Phenological Eyes Network

We obtained hourly digital photographs from six sites of the PEN during 2015-2016. The geographic distribution and land cover of the selected sites is shown in Figure 1 and 2, respectively. The coordinates and dominant land cover of the selected sites are presented in supplemental Table S1. Among the six selected sites, the Mountain Tsukuba site (MTK) and the Takayama flux site (TKY) are located in mountainous areas, where the photographs were frequently filled with snow and dense fog. To address this issue, we downloaded the hourly photographs between 8:00 and 17:00 local standard time for each day during 2015-2016. In contrast, for the other four sites, we only downloaded the photograph taken at noon as the daily observation.

We extracted greenness time series from digital photographs using the R package "Phenopix" (Filippa et al. 2016). First, we manually delineated the Region of Interest (ROI) for each site to only include the vegetated portion of a photograph in the analyses. The delineated ROIs for the selected PEN site are shown in Figure 2. We delineated a single ROI for each site except for the Mase flux site (MSE), where we delineated three ROIs: rice field in the foreground (ROI1), rice field in the upper left corner (ROI2), and trees in the background (ROI3) as outlined in Figure 2(d), respectively. This is because the seasonal greenness variation at the MSE site differed substantially among the three ROIs based on an initial visual assessment. For example, the harvest of the rice field in ROI2 was completed earlier than that of the rice field in ROI1 in both 2015 and 2016. Whereas the vegetation canopy in the three ROIs was fully exposed to the satellite's field of view, the rice field in the foreground occupied the dominant portion of the photograph. Therefore, if we only delineated a single ROI for the MSE site, the differences in the seasonal greenness variation among the three ROIs would be eliminated and the phenology in this highly heterogeneous landscape could not be characterized accurately.

We then calculated the Green Chromatic Coordinate (GCC) for each pixel to represent the vegetation greenness within the delineated ROIs based on equation (3) (Sonnentag et al. 2012):

$$GCC = \frac{G}{R + G + B} \quad (3)$$

where R, G and B represent the digital number from the red, green and blue channels, respectively.

The GCC for a ROI was further calculated by averaging the values over all the pixels enclosed by the ROI, which was then used to generate the time series of three-day GCC for each ROI during 2015-2016. Specifically, if hourly photographs were used to calculate GCC (i.e., MTK and TKY), the three-day GCC was determined using the 90$^{th}$ percentile of all the hourly GCC in a three-day period (Sonnentag et al. 2012; Toomey et al. 2015). In contrast, the maximum GCC from a given three-day period was determined as the three-day GCC if daily photographs were used (i.e., FHK, MSE, TGF and TSE). For each three-day period, we also generated a snow label by visual interpretation of the digital photographs. A label of “snow-present” was denoted only if snow was present in all of the three days otherwise the three-day period was labelled as “snow-free”. We also generated a snow label for each eight-day period to match the temporal resolution of the aggregated MODIS EVI2 time series.

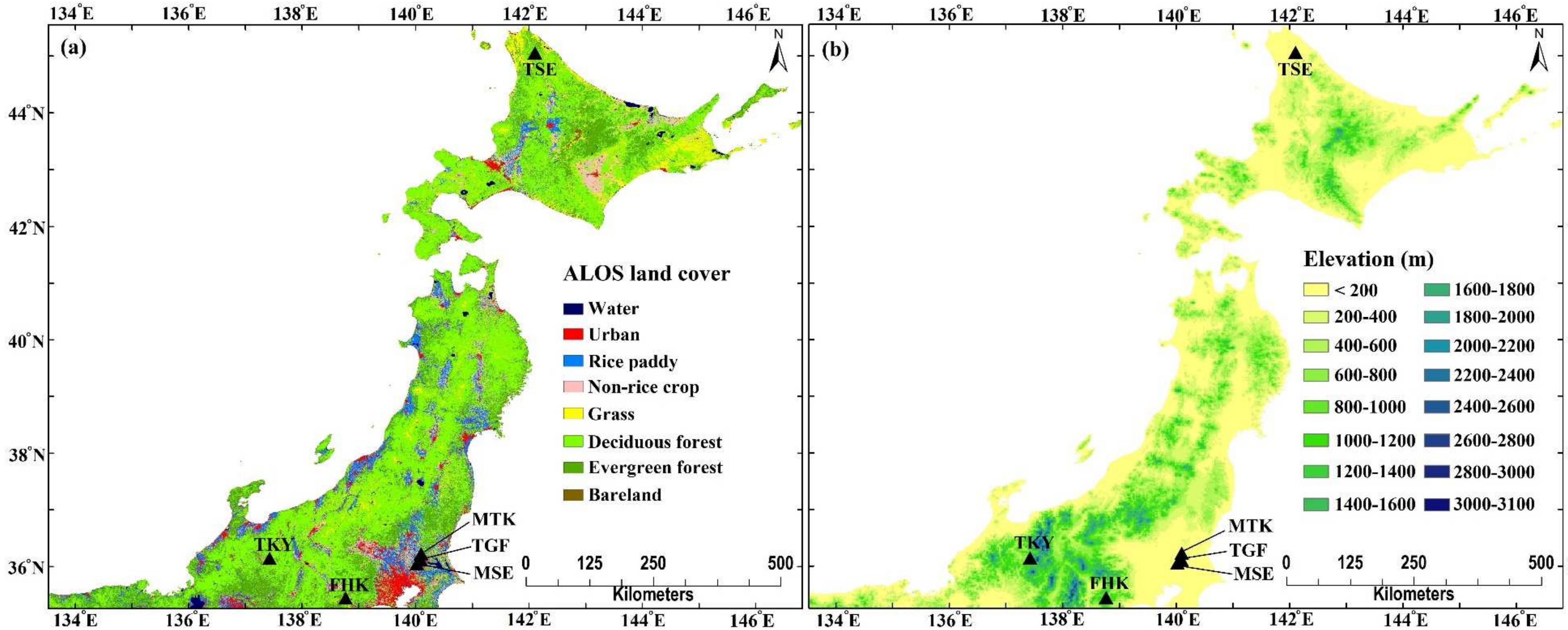


**Figure 1**. The spatial variations in land cover and elevation across central and northern Japan. Black triangles represent the locations of the six selected PEN sites. The land cover map of Japan is derived from data obtained by the Advanced Land Observing Satellite (ALOS), the original data of which is provided by JAXA: http://www.eorc.jaxa.jp/ALOS/en/lulc/lulc_index.htm (©JAXA).

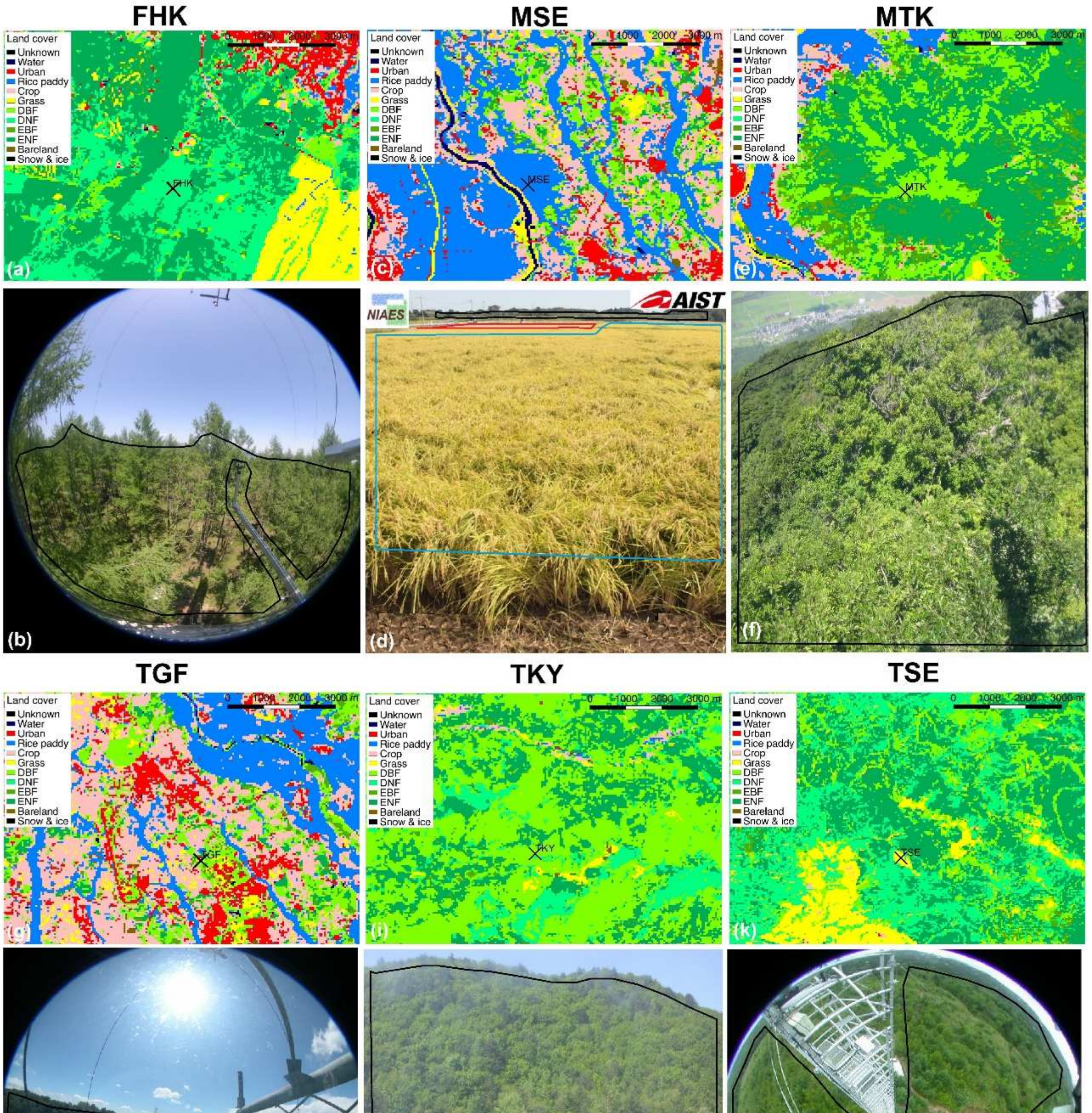


**Figure 2**. Land cover maps (first and third rows) and delineated ROI(s) (second and fourth rows) for selected PEN site. The land cover map is derived from data obtained by the Advanced Land Observing Satellite (ALOS), the original data of which is provided by JAXA: http://www.eorc.jaxa.jp/ALOS/en/lulc/lulc_index.htm (©JAXA). Solid black lines outline the delineated ROIs and the black cross on the land cover map represents the location of corresponding PEN site.

**2.5** Detection of phenological transition dates from AHI, MODIS and PEN data

We used the Hybrid Piecewise Logistic Model-Land Surface Phenology Detection (HPLM-LSPD) algorithm (Zhang 2015; Zhang et al. 2003) to detect the four phenological transition dates (PTDs hereafter) from three-day PEN GCC, eight-day MODIS EVI2, and three-day AHI EVI2 time series, respectively. The four PTDs are Start of Spring (SOS), End of Spring (EOS), Start of Fall (SOF) and End of Fall (EOF) (Zhang et al. 2018a). SOS refers to the onset of rapid greenness increase in early spring whereas EOS represents the timing when greenness starts to reach a maximum level or in other words, the end of greenup phase (Zhang et al. 2003). In contrast, SOF corresponds to the timing when greenness starts to undergo gradual decreases whereas EOF represents the timing when plant canopy reaches the dormancy status or in other words, the greenness minimum (Zhang et al. 2003; Liu et al. 2017).

The following is a brief description of how HPLM-LSPD was used to detect PTDs in this study and a general term of vegetation index (VI) was used to refer to PEN GCC, MODIS EVI2, and AHI EVI2 in the following description. For each AHI and MODIS pixel or PEN ROI, we applied the HPLM-LSPD algorithm in four steps (Zhang 2015). (1) We first determined the background VI as the mean value of the five largest good quality VI values during the dormancy period that was defined as the time period when LST was lower than 5°C. (2) We then smoothed the VI time series by filling the gaps due to missing or low-quality observations. The irregular VI values were then smoothed using the Savitzky-Golay filter (Chen et al. 2004) and a local median filter. (3) We further fitted logistic curves to the smoothed VI time series to reconstruct the VI temporal trajectory. (4) Finally, we calculated the rate of change in curvature from the reconstructed VI temporal trajectory. The four PTDs correspond to the local extreme values of the rate of change in the curvature of the reconstructed VI trajectory (Zhang et al. 2003).

Note that since LST and the information of snow presence/absence serve as important ancillary data in detecting PTDs using HPLM-LSPD algorithm, the MODIS LST and the snow presence/absence information derived from PEN imagery (described in detail in Section 2.4) were employed in the detection of PTDs from VI time series of AHI, MODIS and PEN at the six study sites. We did not use satellite-derived snow presence/absence information because we believe the PEN imagery can provide sufficiently accurate snow presence/absence information given the relatively fine spatial scale of our study (~2km). This is also to make sure that any differences in the PTDs derived from different sensors are results of the differences in VI rather than those in the ancillary data. In contrast, the MODIS snow cover and LST were used in detecting PTDs from AHI data at locations other than the six sites.

For a given PEN site, if more than one ROI was delineated on the digital photographs, the HPLM-LSPD algorithm was applied for each ROI separately, and the mean value of each PTD was calculated for that site. Note that one additional step was taken to determine GCC-derived EOF for the two rice field ROIs delineated for the MSE site in 2016. Specifically, after the rice fields were harvested, green sprouts from the remaining rice stubbles were seen for a very brief period before the fields were plowed (supplemental Figure S1). We therefore replaced the EOF determined using HPLM-LSPD with the plowing day.

**2.6** Characterizing the spatial patterns of phenological transition dates

We obtained land cover and elevation data to facilitate the characterization of the spatial variations in PTDs among different types of land cover, and across elevation and latitudinal gradients. Specifically, we downloaded the land cover product derived from observations acquired by the Advanced Visible and Near Infrared Radiometer type 2 (AVNIR-2) onboard the Advanced Land Observing Satellite (ALOS) (Hashimoto et al. 2014). The ALOS land cover product has a 10m spatial resolution and can be accessed via: https://www.eorc.jaxa.jp/ALOS/en/lulc/lulc_index.htm. We chose the ALOS land cover product because it has ‘rice paddy’ as an individual land cover class, which is a very important land cover in central and northern Japan, and has different plough/harvest schedules from other crops. In addition to rice paddy, we also focused on the following five types of land cover: urban, non-rice crop, grass, deciduous forest and evergreen forest. We obtained the elevation data for our study area by downloading the GTOPO30 digital elevation model from the U.S. Geological Survey EarthExplorer (https://earthexplorer.usgs.gov/). The GTOPO30 digital elevation model has a spatial resolution of 30 arc-second. We then resampled the land cover and elevation data to 0.02 degree using a nearest neighbor method to match the spatial resolution of detected PTDs. We further divided our study area into low (0-200m), medium (200-500m) and high (500-3100m) elevation zones, so that each zone has one third of the total 0.02° grid cells in our study area. In order to examine the PTD changes across latitudes, we divided our study area into low (35°N-38.5°N), medium (38.5°N-42°N) and high (42°N-45.5°N) latitudinal zones. Finally, we examined the relationship between land cover and PTD outliers. For example, the outliers in SOS were determined based on the following two steps. We first sorted the 0.02° grid cells in our study area in ascending order based on their average SOS timing during 2015-2016. We then determined the grid cells that fell below the $10^{th}$ percentile or lay above the $90^{th}$ percentile of the SOS timing as outliers. Then, for any given land cover, we generated a measure of its tendency in being SOS outliers by dividing the number of grid cells from this land cover and classified as SOS outliers to the total number of 0.02° grid cells of this land cover in the study area. We also repeated this analysis for the other three PTDs.

### **2.7** Evaluation of AHI phenological transition dates against those from MODIS and PEN

We evaluated the PTDs detected from AHI EVI2 by comparing them with those detected from MODIS EVI2 and PEN GCC time series. Taking SOS that was derived from PEN ($SOS_{PEN}$) and AHI data ($SOS_{AHI}$) as an example of the evaluation analyses, we first calculated the Root Mean Square Difference (RMSD) and Bias between $SOS_{PEN}$ and $SOS_{AHI}$ across the six sites in 2015 and 2016. We then conducted linear regression analyses by using $SOS_{AHI}$ as the dependent variable and $SOS_{PEN}$ as the independent variable to retrieve the R-square ($R^2$) and statistical significance (p value). These analyses were repeated for the other three PTDs (EOS, SOF, and EOF), and between MODIS and PEN PTDs. In addition, the linear regression analyses were also conducted between PTDs detected from AHI and MODIS data with a given PTD from AHI and MODIS as the independent and dependent variable, respectively.

## **3. Results**

### **3.1** Spatial patterns of the phenological transition dates detected from AHI EVI2 time series

Figures 3-6 present the general spatial patterns of the four PTDs along with their variations among different types of land cover, and across elevation and latitudinal gradients. The average timing of SOS during 2015-2016 primarily fell between late March and early May (Figure 3a). The direction of changes in SOS timing across elevation and latitudinal gradients varies with land cover. Specifically, SOS timing of grass, deciduous and evergreen forests exhibited delays with increases in either elevation or latitude (Figure 3b-3d). For urban, rice paddy and non-rice crop, however, delays in SOS timing associated with increasing elevation only occurred in the high latitude zone (Figure 3b). Meanwhile, delays in SOS timing associated with increases in latitude were only found for non-rice crop, rice paddy in the high elevation zone, and urban areas in the medium and high elevation zones (Figure 3b-3d). The average timing of EOS during 2015-2016 predominately fell in the period from mid-May to mid-July (Figure 4a). In contrast to SOS timing, EOS timing exhibited advances with increasing elevation, especially in the low and medium latitude zones (Figure 4c and 4d). In addition, for a given type of land cover within a given elevation zone, EOS timing did not exhibit consistent changes across latitudes except the delayed EOS of deciduous forest in the medium elevation zone. The average timing of SOF during 2015-2016 primarily fell between mid-August and early October (Figure5a). There were no distinct changes in SOF timing across elevation gradients except for rice paddy and non-rice crop in the low latitude zone (Figure 5d), and urban area in the high latitude zone (Figure 5b). In addition, for a given type of land cover within a given elevation zone, SOF timing in the high latitude zone tended to be much earlier than those in the low and medium latitude zones. The average timing of EOF during 2015-2016 predominately fell in the period from early November to late December (Figure 6a). In contrast to SOS timing, the EOF timing of grass, deciduous and evergreen forests exhibited advances with increases in either elevation or latitude (Figure 6b-6d). For urban, rice paddy and non-rice crop, changes in EOF timing across latitudinal gradients were more distinct than those across elevation gradients. Specifically, advances in EOF timing with increasing latitudes were found for all six types of land cover in almost all elevation zones while consistent changes in EOF timing across elevation gradients were only found in urban area in the low latitude zone, and non-rice crop in the high latitude zone. Figure 7 presents the variations in the percentage of 0.02° grid cells from a given land cover class being outliers for each of the four PTDs. Urban and rice paddy were the two land cover classes that had the highest percentage of grid cells being outliers for SOS, EOS and EOF (Figure 7a, 7b and 7d). Evergreen forest and urban had the highest percentage of grid cells being outliers for SOF (Figure 7c). In contrast, grass and deciduous forest had the lowest percentage of grid cells being outliers for all of the four PTDs.

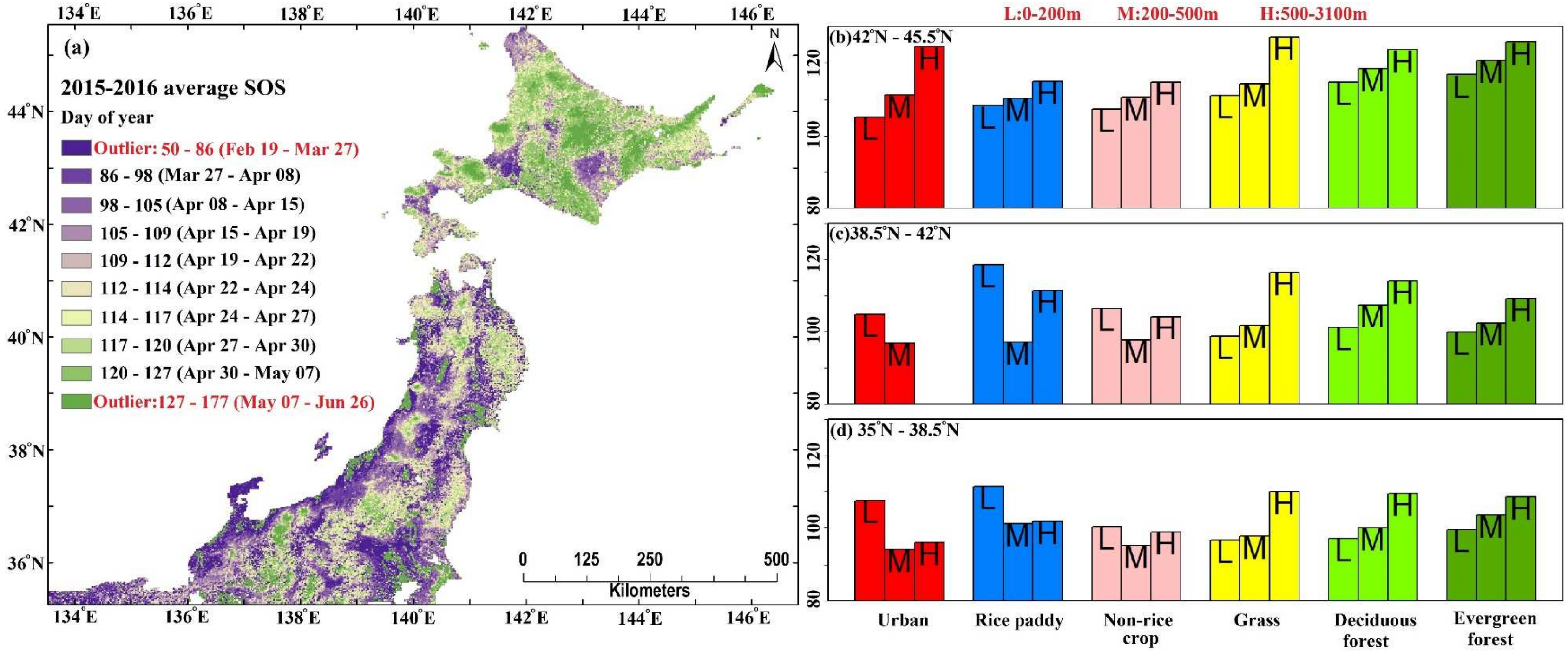


**Figure 3**. Spatial pattern of the average SOS detected in 2015 and 2016 (a), and the variations in the average SOS among different types of land cover, and across latitudinal and elevation gradients (b-c). In Panel (a), each color bar in the legend represents 10% of the total number of 0.02° grid cells in the study area. Panel (b), (c) and (d) represents grid cells located in the high (42°N-45.5°N), medium (38.5°N-42°N) and low (35°N-38.5°N) latitude zones, respectively. Each bar represents the mean value of SOS for grid cells from a given type of land cover within a given elevation zone. The standard deviation associated with each bar is presented in supplemental Table S2. The label 'L' and 'M' and 'H' represents the low (0-200m), medium (200-500m) and high (500-3100m) elevation zones, respectively.

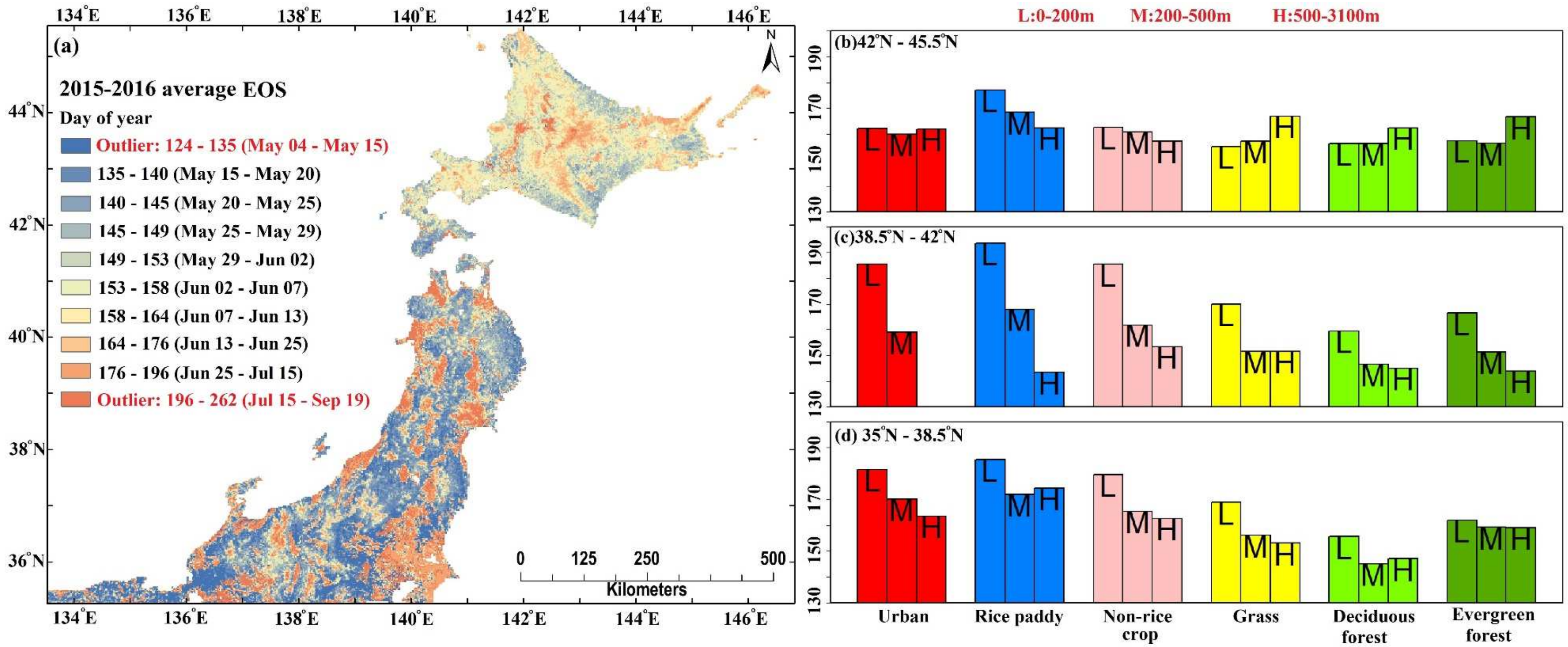


**Figure 4**. Spatial pattern of the average EOS detected in 2015 and 2016 (a), and the variations in the average EOS among different types of land cover, and across latitudinal and elevation gradients (b-c). In Panel (a), each color bar in the legend represents 10% of the total number of 0.02° grid cells in the study area. Panel (b), (c) and (d) represents grid cells located in the high (42°N-45.5°N), medium (38.5°N-42°N) and low (35°N-38.5°N) latitude zones, respectively. Each bar represents the mean value of EOS for grid cells from a given type of land cover within a given elevation zone. The standard deviation associated with each bar is presented in supplemental Table S3. The label 'L' and 'M' and 'H' represents the low (0-200m), medium (200-500m) and high (500-3100m) elevation zones, respectively.

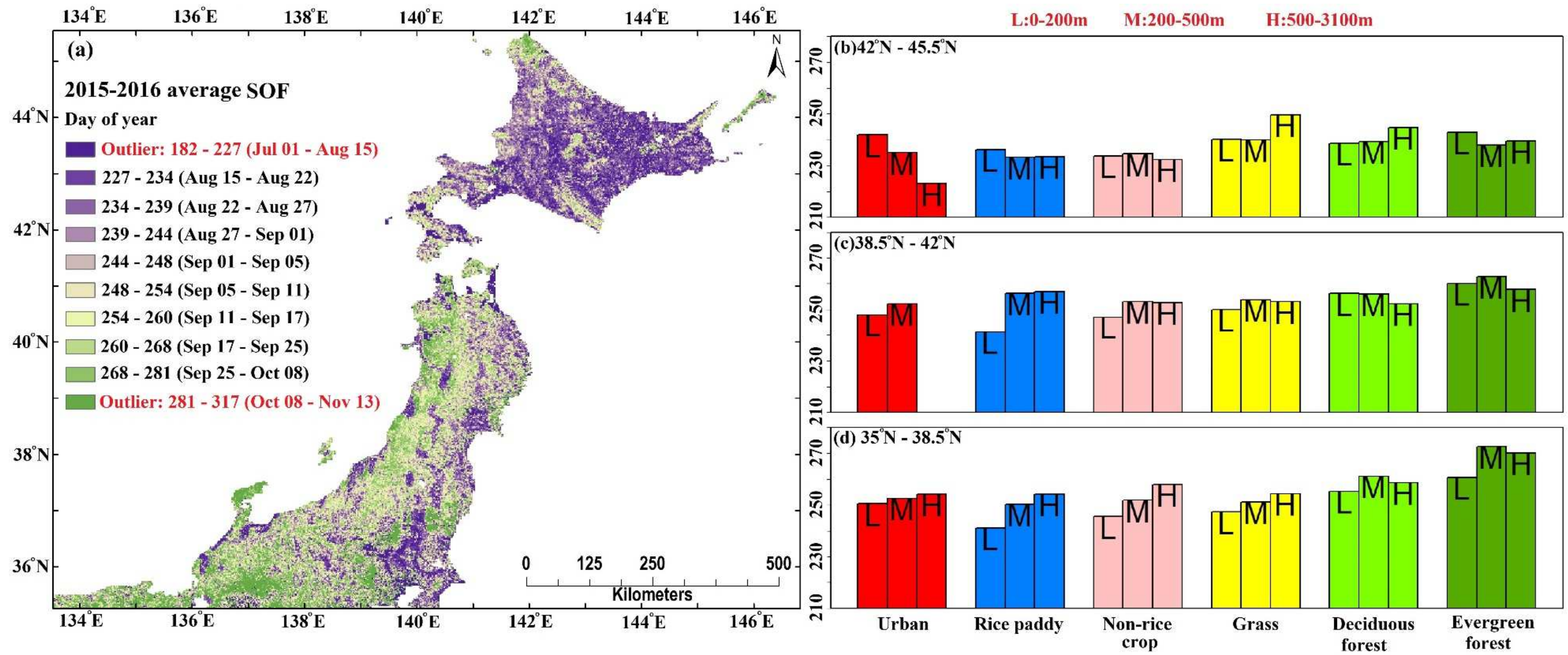


**Figure 5**. Spatial pattern of the average SOF detected in 2015 and 2016 (a), and the variations in the average SOF among different types of land cover, and across latitudinal and elevation gradients (b-c). In Panel (a), each color bar in the legend represents 10% of the total number of 0.02° grid cells in the study area. Panel (b), (c) and (d) represents grid cells located in the high (42°N-45.5°N), medium (38.5°N-42°N) and low (35°N-38.5°N) latitude zones, respectively. Each bar represents the mean value of SOF for grid cells from a given type of land cover within a given elevation zone. The standard deviation associated with each bar is presented in supplemental Table S4. The label 'L' and 'M' and 'H' represents the low (0-200m), medium (200-500m) and high (500-3100m) elevation zones, respectively.

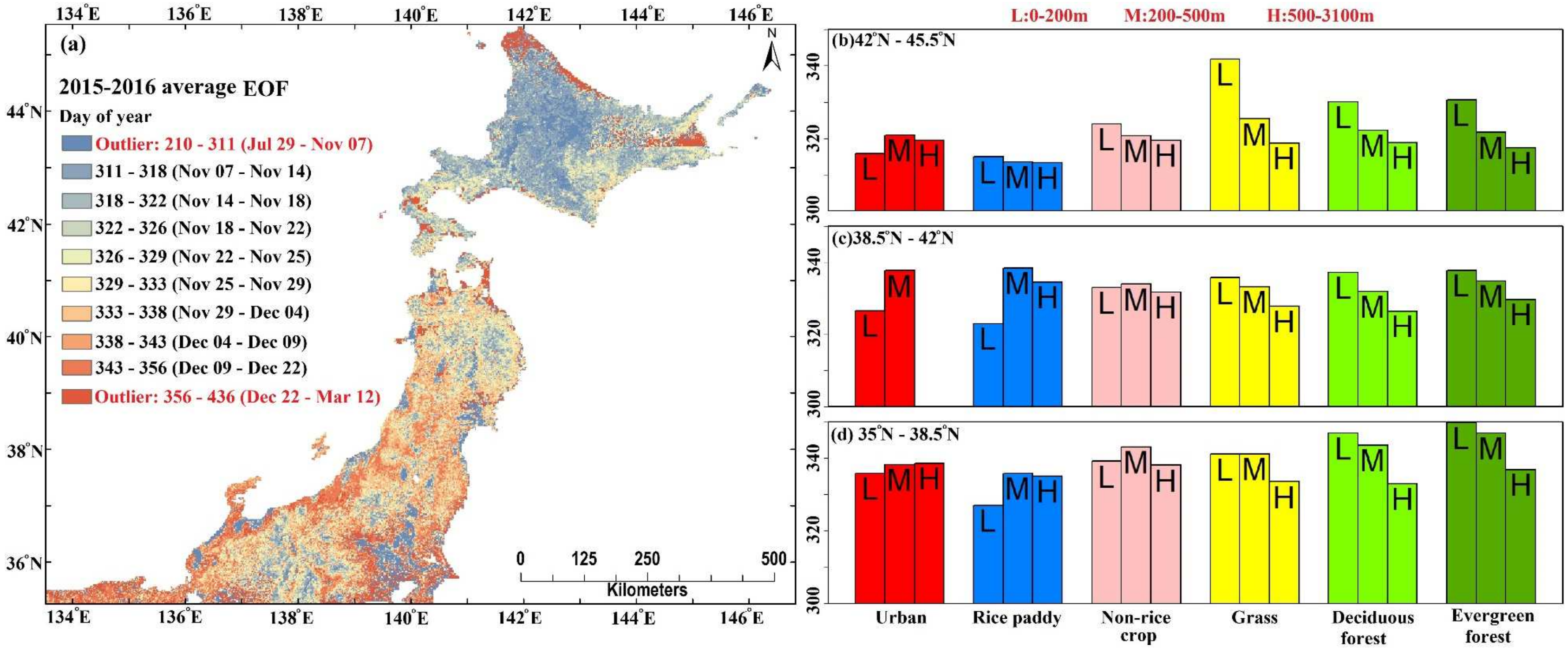


**Figure 6**. Spatial pattern of the average EOF detected in 2015 and 2016 (a), and the variations in the average EOF among different types of land cover, and across latitudinal and elevation gradients (b-c). In Panel (a), each color bar in the legend represents 10% of the total number of 0.02° grid cells in the study area. Panel (b), (c) and (d) represents grid cells located in the high (42°N-45.5°N), medium (38.5°N-42°N) and low (35°N-38.5°N) latitude zones, respectively. Each bar represents the mean value of EOF for grid cells from a given type of land cover within a given elevation zone. The standard deviation associated with each bar is presented in supplemental Table S5. The label 'L' and 'M' and 'H' represents the low (0-200m), medium (200-500m) and high (500-3100m) elevation zones, respectively.

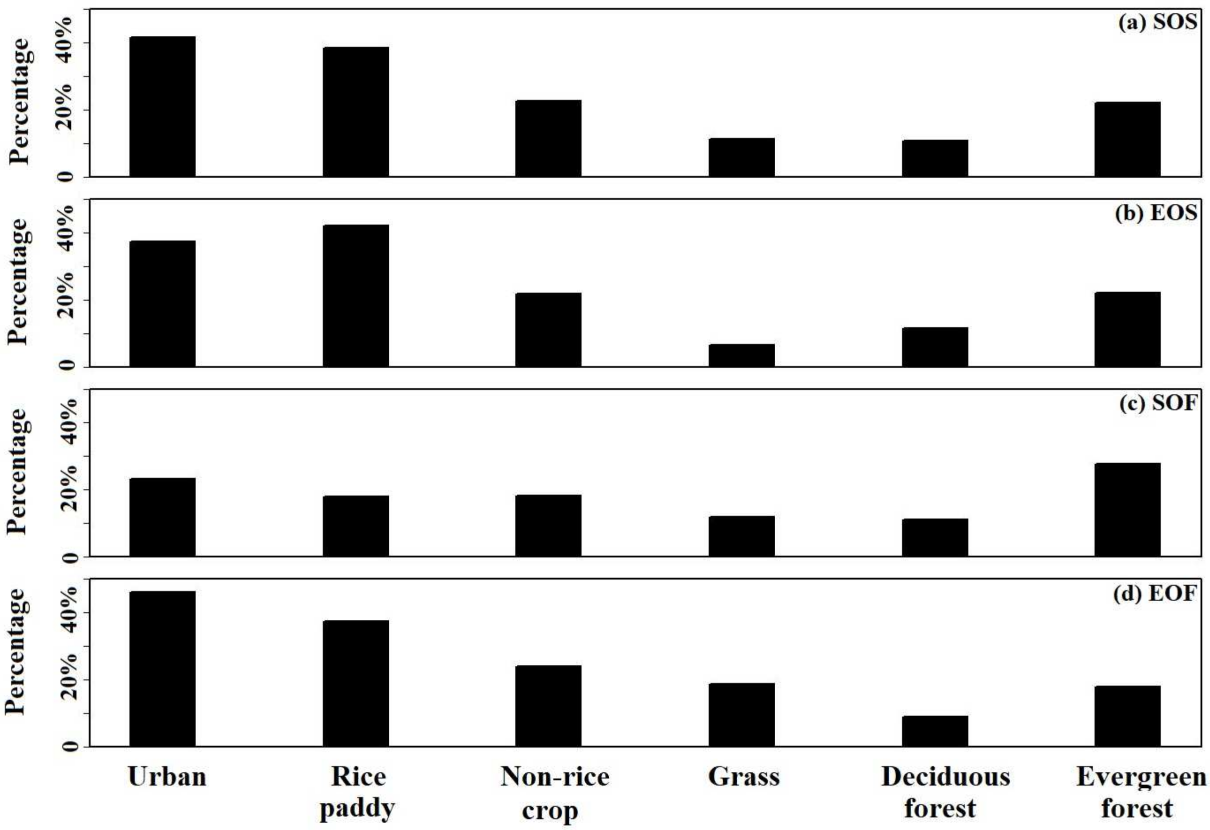


**Figure 7**. Variations in the percentage of the 0.02° grid cells from a given land cover class being outliers for SOS (a), EOS (b), SOF (c) and EOF (d).

**3.2** Differences in the greenness trajectories and detected phenological transition dates from AHI, MODIS and PEN data

Figure 8 presents the original and reconstructed time series of PEN GCC, MODIS EVI2, and AHI EVI2 during 2015 and 2016 at the six PEN sites. Their temporal patterns were generally similar albeit the distinct differences between the original GCC and EVI2 time series. For example, at the three forest sites in central Japan (i.e., FHK, MTK and TKY), the original GCC time series showed substantial decreases during summer whereas the original MODIS and AHI EVI2 time series maintained a relatively stable plateau (Figure 8a, 8c and 8e). In addition, the short-term disturbance that was picked up by the GCC time series at MSE (i.e., the abrupt GCC decrease in ROI1 during late 2016) and TGF (i.e., the rapid decrease and recovery of greenness in the middle of 2015 and 2016) were not visible in both the MODIS and AHI EVI2 time series. Note that the GCC time series from the other two ROIs at MSE can be found in supplemental Figure S2.

Table 1 summarizes the bias and RMSD between the PTDs derived from PEN and satellite data. Specifically, $SOS_{AHI}$ occurred as long as 16 days before $SOS_{PEN}$ at TGF in 2015 whereas the longest advance of $SOS_{MODIS}$ relative to $SOS_{PEN}$ was 22 days at MTK in 2015. Both $SOS_{AHI}$ and $SOS_{MODIS}$ showed the longest delay relative to $SOS_{PEN}$ at MSE in 2016 with the delay being 21 and 27 days, respectively. The longest advance of satellite-derived EOS relative to that derived from PEN occurred at TSE in 2015 with $EOS_{AHI}$ and $EOS_{MODIS}$ occurring 23 and 26 days before $EOS_{PEN}$, respectively. Relative to $EOS_{PEN}$, the longest delay in satellite-derived EOS was 38 days for AHI at TGF in 2016, and 68 days for MODIS at TKY in 2015. The difference in SOF ranged from $SOF_{AHI}$ and $SOF_{MODIS}$ occurring 57 and 59 days in advance of $SOF_{PEN}$, respectively, at TKY in 2016 to 39 and 38 days behind $SOF_{PEN}$ at TSE in 2016 and at TGF in 2015, respectively. $EOF_{AHI}$ consistently occurred after $EOF_{PEN}$ during 2015 and 2016 across the six sites with a minimum and maximum delay of four days at TSE in 2015 and 45 days at MTK in 2015, respectively. In contrast, the difference between $EOF_{MODIS}$ and $EOF_{PEN}$ ranged from $EOF_{MODIS}$ occurring 23 days before $EOF_{PEN}$ at TSE in both 2015 and 2016 to $EOF_{MODIS}$ occurring 35 days after $EOF_{PEN}$ at MSE in 2015.

In Table 1, the direction of the overall bias of satellite-derived PTDs relative to those derived from PEN imagery were consistent between AHI and MODIS, except for SOS. For AHI, the overall bias ranged from SOF occurring 15 days before PEN-derived SOF to EOF occurring 22 days behind PEN-derived EOF. For MODIS, the overall bias ranged from SOF occurring 4 days before PEN-derived SOF to EOS occurring 23 days behind PEN-derived EOS.

The RMSD between satellite-derived and PEN-derived PTDs (Table 1) were lower in spring (i.e., SOS and EOS) than that during fall (i.e., SOF and EOF). In addition, the RMSD between PTDs derived from AHI and PEN were smaller than those between PTDs from MODIS and PEN for SOS and EOS (i.e., during the green-up phase). In contrast, the RMSD between PTDs derived from AHI and PEN were comparable to those between PTDs from MODIS and PEN for SOF and EOF (i.e., during the senescence phase).

Figure 9 displays the correlation between the spatiotemporal variability in PTDs derived from each two of PEN, MODIS, and AHI during 2015 and 2016 across the six sites. Except SOF, the PEN and AHI PTDs were significantly correlated ($p < 0.05$) with the highest $R^2$ of 0.75 between PEN and AHI-derived SOS (Figure 9a-9d). In contrast, significant correlations were only found between PEN and MODIS SOS and EOF with an $R^2$ of 0.46 and 0.41, respectively (Figure 9e-9h). Similarly, for AHI and MODIS PTDs, significant correlations were only found between SOS and EOF with an $R^2$ of 0.59 and 0.57, respectively (Figure 9i-9l). A complete summary of the regression statistics can be found in supplemental Table S6.

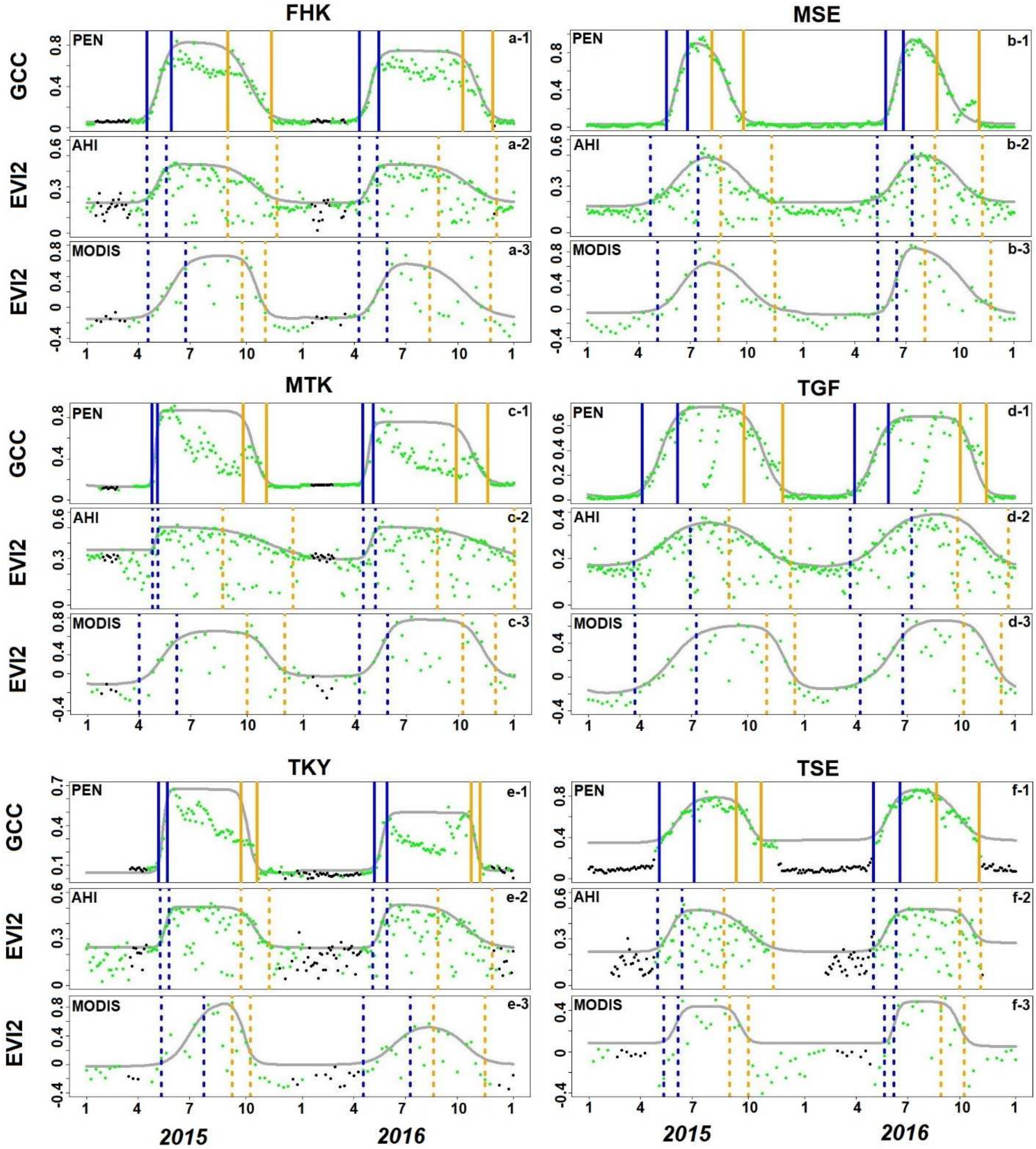


**Figure 8**. Comparison of greenness trajectories and PTDs derived from EVI2 with those from GCC at the six sites during 2015-2016. Solid green and black circles represent the original snow-free and snow-affected EVI2/GCC, respectively. The grey solid lines represent the reconstructed greenness trajectories. The blue dashed lines represent the detected SOS and EOS whereas orange dashed lines represent SOF and EOF.

Table 1. A comparison of the four PTDs detected from GCC with those derived from EVI2 time series (e.g., $\Delta SOS_{AHI} = SOS_{AHI} - SOS_{PEN}$ and $\Delta SOS_{MOD} = SOS_{MODIS} - SOS_{PEN}$). Positive (negative) bias indicates a PTD derived from satellite data is later (earlier) than that derived from PEN imagery. All the numbers have been rounded to the nearest integer.

| | | **$SOS_{PEN}$** | **$\Delta SOS_{AHI}$** | **$\Delta SOS_{MOD}$** | **$EOS_{PEN}$** | **$\Delta EOS_{AHI}$** | **$\Delta EOS_{MOD}$** | **$SOF_{PEN}$** | **$\Delta SOF_{AHI}$** | **$\Delta SOF_{MOD}$** | **$EOF_{PEN}$** | **$\Delta EOF_{AHI}$** | **$\Delta EOF_{MOD}$** |
|---|---|---|---|---|---|---|---|---|---|---|---|---|---|
| **FHK** | 2015 | 104 | -1 | 1 | 145 | -7 | 26 | 243 | 0 | 28 | 317 | 10 | -8 |
| | 2016 | 103 | 0 | -2 | 136 | -3 | 12 | 278 | -41 | -58 | 329 | 7 | 0 |
| **MSE** | 2015 | 111 | -1 | 10 | 155 | 35 | 33 | 226 | 3 | 2 | 287 | 31 | 35 |
| | 2016 | 111 | 21 | 27 | 162 | 29 | 7 | 230 | 2 | -12 | 298 | 13 | 28 |
| **MTK** | 2015 | 112 | 2 | -22 | 123 | -1 | 33 | 269 | -37 | 10 | 307 | 45 | 31 |
| | 2016 | 107 | 1 | -2 | 126 | 2 | 26 | 267 | -33 | 10 | 322 | 43 | 15 |
| **TGF** | 2015 | 95 | -16 | -10 | 156 | 21 | 35 | 270 | -29 | 38 | 335 | 13 | 25 |
| | 2016 | 94 | -10 | 8 | 151 | 38 | 23 | 272 | -4 | 8 | 317 | 36 | 25 |
| **TKY** | 2015 | 124 | 3 | 12 | 139 | 5 | 68 | 265 | 1 | -12 | 292 | 21 | -6 |
| | 2016 | 129 | -4 | -17 | 150 | 1 | 45 | 293 | -57 | -59 | 310 | 20 | 10 |
| **TSE** | 2015 | 123 | -3 | 8 | 183 | -23 | -26 | 253 | -21 | -9 | 296 | 22 | -23 |
| | 2016 | 124 | -2 | 16 | 169 | -7 | -7 | 230 | 39 | 11 | 303 | 4 | -23 |
| **RMSD** | | | 8 | 14 | | 20 | 33 | | 29 | 29 | | 26 | 22 |
| **Overall Bias** | | | -1 | 2 | | 8 | 23 | | -15 | -4 | | 22 | 9 |

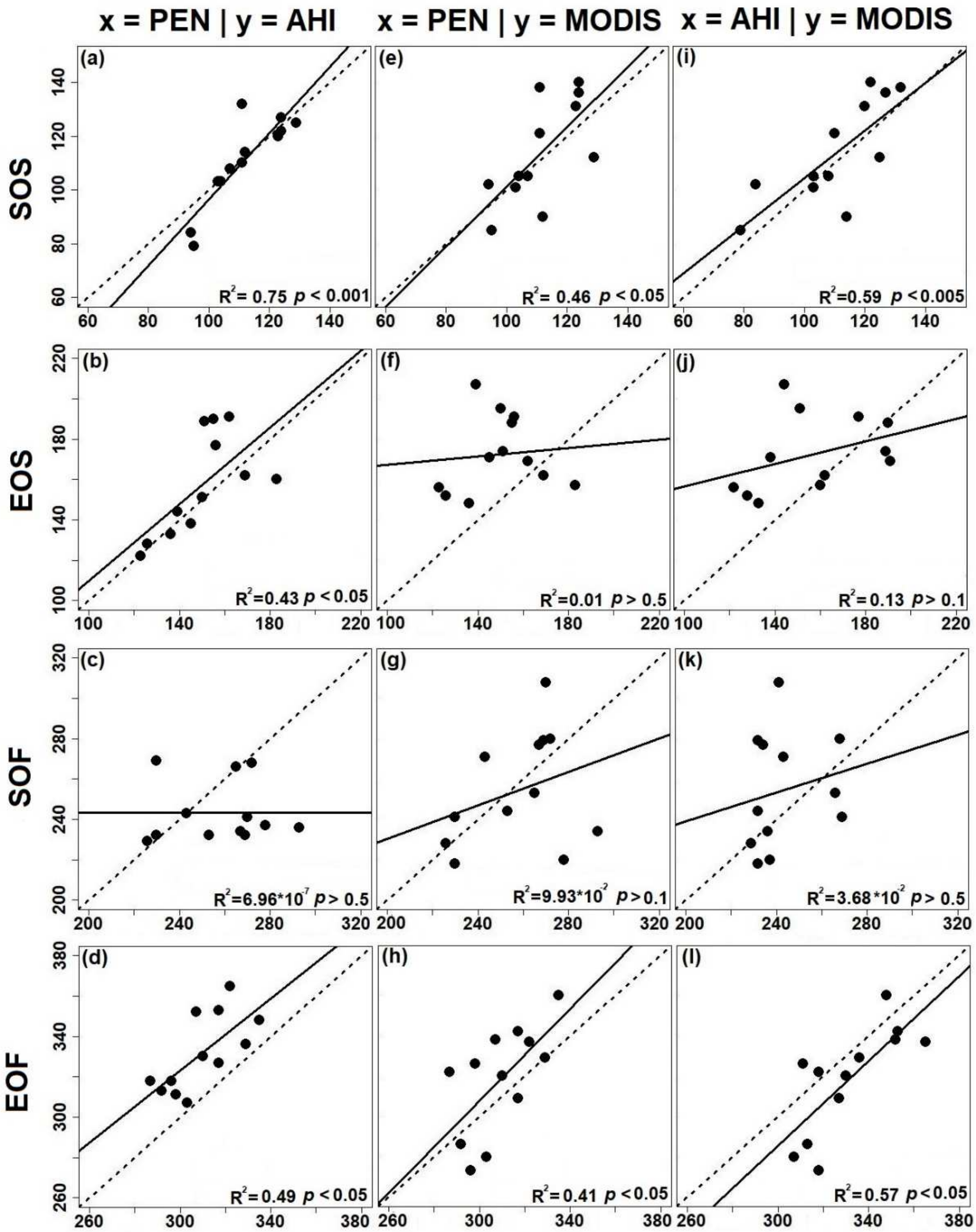


**Figure 9**. Regressions of PTDs detected from PEN and satellite data during 2015 and 2016 across the 12 sites. The dotted line represents the 1:1 line while the solid line represents the fitted regression line.

## 4. Discussion

**4.1** The anthropogenic footprints on the spatial variations in SOS and EOF in central and northern Japan

The results from the analyses on the spatial variations in SOS and EOF (Figures 3, 6 and 7) highlight the anthropogenic footprints in the study area. In the mid-latitude region of the northern hemisphere, temperature plays one of the most important role in mediating the timing of SOS and EOF(Zhang et al. 2004a). In central and northern Japan, the spatial variations of SOS and EOF timing in grass, deciduous and evergreen forests were consistent with temperature changes across gradients in either latitude or elevation, which is in agreement with findings from multiple studies (Zhang et al. 2004a; Xie et al. 2017; An et al. 2018). In urban areas and croplands, however, the spatial variations of SOS and EOF timing were only consistent with changes in temperature across gradients in latitude and elevation in certain parts of the study area. This can be explained by that while the SOS and EOF of grass, deciduous and evergreen forests are predominately mediated by temperature, the "urban heat island" effect associated with altered surface albedo and increased aerosols can affect the temperature regime (Krehbiel et al. 2017), and management practices are likely more important than temperature in mediating SOS and EOF timing in croplands of the study area (Suepa et al. 2016). Numerous previous studies have also reported the significant impacts from anthropogenic activities such as urbanization and irrigation on SOS and EOF of urban areas (Zhang et al. 2004b; Buyantuyev & Wu 2012; Walker et al. 2015; Krehbiel et al. 2017) and croplands (Sakamoto et al. 2006; Suepa et al. 2016), respectively. The changes in the percentage of grid cells being outliers for SOS and EOF in Figure 7 also demonstrates the impacts from anthropogenic activities. Specifically, urban areas and croplands had higher percentage of grid cells being outliers for SOS and EOF than those from grass, deciduous and evergreen forests. In addition, although grass in the study area tended to have very low percentage of grid cells being SOS and EOF outliers, some very noticeable EOF outliers occurred in the grass-dominated coastal areas of northern Japan (Figure 6a). By examining a high-resolution Google Earth image of this area, we speculated that these grass-dominated areas were managed for livestock grazing purposes (supplemental Figure S3). Therefore, the very late EOF timing in these areas likely resulted from the management practices favorable for longer growing seasons.

In contrast to SOS and EOF, no distinct differences were found between the naturally vegetated areas (i.e., grass, deciduous and evergreen forests), and urban and croplands in terms of the spatial variations in EOS and SOF across the gradients in latitude and elevation (Figures 4 and 5). Furthermore, the spatial variations in EOS and SOF were much more complicated than those in SOS and EOF. One likely explanation is that, the spatial variations in other environmental factors such as water availability also affect those in EOS and SOF. Since few previous studies have focused on the mediating factors of variations in EOS and SOF across spatial gradients, this subject needs thorough examinations in future studies.

**4.2** Impacts of atmospheric effects and land surface disturbances on the reconstruction of greenness trajectories

Substantial decreases in GCC during summer were evident at the two mountainous sites MTK and TKY (Figure 8). By reviewing the photograph archives, it was found that the GCC decrease owed to the atmospheric effects such as dense fog or high humidity accumulation on camera lens (supplemental Figure S4-S5). These atmospheric effects also affected the time series of AHI and MODIS EVI2 resulting in the low EVI2 values. However, unlike the continuously low PEN GCC, the AHI EVI2 time series were able to maintain a relatively stable plateau during the same time period. This is because the GCC time series was generated from hourly observations while the AHI EVI2 time series was generated from observations at a 20-mintue interval. Therefore, AHI EVI2 had higher chances of acquiring observations free of significant atmospheric impacts (supplemental Figure S4-S5). In contrast, no prolonged cloudy or foggy conditions were identified at FHK, where the GCC decrease during summer was likely related to the reduced contrast between reflectance from green and red wavelengths (Elmore et al. 2012). At MSE and TGF, abrupt changes occurred in the GCC time series. The abrupt GCC changes at MSE was due to the removal of green sprouts from rice stubbles in late October of 2016 (supplemental Figure S1) whereas the quick decrease and recovery in GCC in the middle of 2015 and 2016 at TGF were due to the removal of grasses and the rapid regrowth afterwards (supplemental Figure S6). These land surface disturbances were mainly restricted to the region close to MSE and TGF, which only accounted for a small portion of the corresponding MODIS and AHI pixels. As a result, the local abrupt greenness changes had little influences on MODIS and AHI EVI2 time series.

Although noisy data appeared in the original time series of PEN GCC, MODIS EVI2, and AHI EVI2, the HPLM-LSPD algorithm is able to reconstruct the greenness trajectories and detect the phenological transitions. This is due to the fact that the HPLM-LSPD algorithm reconstructs a greenness trajectory by following the upper boundary of the greenness time series (Zhang 2015), which would automatically filter out the low values typically associated with atmospheric effects and land surface disturbances. In addition, it has been demonstrated that reconstruction of greenness trajectory using the HPLM-LSPD algorithm is reliable as long as there is one good quality observation every eight days (Zhang et al. 2009). Snow cover and land surface temperature data are important ancillary data in PTD detection using the HPLM-LSPD algorithm (Zhang 2015). Although we used MODIS snow and land surface temperature products to facilitate the detection of PTDs from AHI EVI2 time series, it is also possible to generate these two types of ancillary data from AHI observations. Specifically, the Normalized Difference Snow Index, which is used to generate the MODIS snow product (Riggs et al. 1994), can also be derived from AHI Band 2 (0.51 μm) and 5 (1.61 μm). In addition, a land surface temperature retrieval algorithm using AHI data has also been developed in a recent study (Choi & Suh 2018).

### **4.3** The impacts of the difference between phenological changes in spring and fall on LSP monitoring using PEN and satellite data.

The RMSD between PTDs derived from PEN and satellite data during 2015-2016 across the six study sites reveals an interesting contrast between spring and fall phenology. For example, the RMSD for AHI increased from 8 (SOS) and 20 (EOS) days in spring to 26 (EOF) and 29 (SOF) days in fall. The RMSD for MODIS-derived PTDs had similar variations, which ranged from 14 (SOS) and 33 (EOS) days in spring to 22 (EOF) and 29 (SOF) days in fall. This is consistent with the findings from previous studies in which PTDs derived from digital cameras are used as the reference to evaluate their counterparts derived from sensors such as Landsat TM and ETM+ (Melaas et al. 2016), MODIS (Hufkens et al. 2012; Klosterman et al. 2014) and VIIRS (Zhang et al. 2018a). The increases in the RMSD between PEN and satellite-derived PTDs from spring to fall can be attributed to the mismatch in the scale of observation coupled with the increased between-canopy variability in phenological changes from spring to fall. Specifically, compared to the green-up phase in spring, there is greater between-canopy difference in the rate of change in leaf coloration during fall (Melaas et al. 2016). Therefore, given the low between-canopy variability in spring, the phenological changes within the small areas observed by the camera can be representative of those in the bigger ground areas related to a satellite pixel. In contrast, the higher between-canopy variability in fall renders greater difference between the phenological changes observed by the camera and the satellite thus leading to higher RMSD.

It is worth noting that the direction of bias in EOS, SOF and EOF relative to those derived from PEN were consistent between AHI and MODIS. Specifically, both AHI-derived and MODIS-derived

EOS were later than PEN-derived EOS by an average of 8 and 23 days, respectively. This is likely due to the different sensitivity of GCC and EVI2 to changes in leaf area index (LAI) over canopies with high LAI. EOS represents the timing when plant canopy reaches maturity during late spring. Results from a previous study on the relationship between GCC and LAI at a temperate deciduous forest site indicate that peak GCC occurs about two weeks in advance of maximum LAI (Keenan et al. 2014). This is similar to the behavior of NDVI, which also has been found to becoming saturated when LAI reaches a certain threshold (Huete et al. 2002; Jiang et al. 2008). In contrast, EVI2 was developed to have enhanced sensitivity over high-LAI canopies (Jiang et al. 2008). For our study sites, it is possible that when canopy LAI reached a certain threshold, GCC became saturated whereas satellite-derived EVI2 was still sensitive to the increasing LAI, which resulted in a later EOS relative to that derived from GCC. This different sensitivity of GCC and EVI2 to LAI dynamics over high-LAI canopies can also be used to explain the earlier SOF derived from EVI2 than that derived from GCC. Specifically, SOF refers to the start of leaf senescence. Therefore, it is possible that while EVI2 was sensitive to the decreases in LAI, GCC stayed being saturated until LAI dropped below a certain threshold, which led to that SOF derived from AHI and MODIS EVI2 occurred earlier than the SOF derived from GCC. The positive bias of satellite-derived EOF relative to the PEN-derived EOF can be explained by that the high between-canopy variability in leaf senescence coupled with the larger ground area associated with a satellite pixel resulted in a slower leaf senescence process than that observed by cameras thus resulting in a delayed EOF relative to that from PEN.

The RMSD for AHI-derived PTDs was no higher than 60% of the RMSD of MODIS-derived PTDs in spring whereas the RMSD for AHI-derived PTDs was equivalent to or even slightly higher that of MODIS-derived PTDs during fall. In other words, PTDs derived from three-day AHI EVI2 time series exhibited improvements over those derived from eight-day MODIS EVI2 time series only during spring, which we believe related to the differences between the limiting factors of LSP detection in spring and fall. Specifically, the six PEN sites included in this study are located in temperate ecosystems with strong deciduousness, the greenup phase of which tends to unfold rapidly therefore generating a strong signal of greenness increases (Hufkens et al. 2012; Melaas et al. 2016; Zhang et al. 2018a). The steep slopes of the greenness trajectories during spring at the three forest sites FHK, MTK and TKY, and at the cropland site MSE in Figure 8 serve as great examples of this rapid greenness increase. As a result, the higher temporal resolution of the AHI EVI2 time series help better characterize this rapid greenness increase, thus led to lower RMSD. In contrast, the greenness decrease in fall tends to be gradual, and more importantly, it is dominated by colors of red, yellow and brown instead of green (Zhang et al. 2018a). Given the slow leaf coloration in fall, it is likely that the temporal resolution of EVI2 time series is no longer the dominant limiting factor. Therefore, since the same vegetation index, EVI2, was used in the detection of PTDs from AHI and MODIS, it is not surprising that there was comparable RMSD for AHI- and MODIS-derived PTDs in fall.

Figure 9 presents the between-sensor comparison of the correlation in the spatiotemporal variability of the four PTDs across the six sites between 2015 and 2016. For each of the three between-sensor comparisons, the correlations were relatively strong for SOS and EOF whereas the correlations for the two mid-season PTDs (i.e., EOS and SOF) were very weak except between AHI- and PEN-derived EOS. We did not find completely consistent results from previous studies. For example, Klosterman et al. (2014) quantifies the correlations between the same four PTDs derived from PhenoCam and MODIS data based on different curve-fitting methods across 13 temperate deciduous sites in the United States (a total of 81 site-years of data). Results show that the $R^2$ for EOS is very similar to that of SOS and EOF while SOF has the lowest $R^2$ among the four PTDs, which ranges from 0.11 to 0.32. Zhang et al. (2018) also quantifies the correlations between the same four PTDs derived from PhenoCam and VIIRS data at 82 sites from the United States (~160 site-years of data). Results show that the $R^2$ is no less than 0.78 for all the four PTDs. We therefore speculate the low $R^2$ for EOS and SOF in our study might be caused by the low number of available samples. This is a limitation of our study and more samples from PEN and satellite data are needed to evaluate SOF and EOS more thoroughly in future studies.

## 5. Conclusion

In this study, we present the first LSP detection results from AHI EVI2 and compare them against those derived from MODIS EVI2 and PEN GCC at six sites in central and northern Japan during 2015-2016. The difference in the spatial variations of SOS and EOF timing between naturally vegetated areas, and urban areas and croplands indicates the anthropogenic footprints on LSP. The spatial variations of EOS and SOF timing are relatively complicated and the mediating factors need to be examined in future studies.

Our results also highlight the advantage of using high-frequency observations from AHI to obtain reliable greenness trajectories in the regions where unfavorable atmospheric conditions can prevail for a prolonged period of time. This indicates that AHI holds great potential to achieve improved LSP detections in other cloud-prone ecosystems in the Asia-Pacific region such as the tropical forests in Southeast Asia. However, our results also show that while the high frequency observations from AHI helped reduce the uncertainty in PTD detections during spring, they did not provide an overall improvement during the leaf senescence phase. This is because leaf phenology is mediated by changes in multiple leaf traits such as LAI, leaf chlorophyll and water content, leaf biomass and photosynthetic rates. Previous studies have shown that there are larger divergence in the changes of these leaf traits during the leaf senescence phase than during the green-up phase (Keenan et al. 2014; Lu et al. 2018). Since greenness indices mainly track changes in LAI and leaf chlorophyll content, they cannot provide a full picture of phenological changes during the leaf senescence phase, even with the increased observation frequency. Therefore, there is a need for using multiple remote sensing perspectives to characterize phenological changes during the leaf senescence phase instead of solely relying on greenness indices. Fortunately, several recently launched and upcoming satellite-borne instruments have the capability to provide insights into leaf senescence phenology that are complementary to those offered by greenness indices. For example, results from Lu et al. (2018) have demonstrated that solar-induced chlorophyll fluorescence (SIF) can better track changes in leaf photosynthesis during the senescence phase than GCC and NDVI in a temperate forest. Therefore, the high frequency SIF measurements from NASA's Geostationary Carbon Observatory (scheduled for launch in the early 2020s) (Moore et al. 2018) and ESA's Tropospheric Monitoring Instrument (TROPOMI, launched in October 2017) (Köehler et al. 2018) are very promising in improving the monitoring of leaf senescence phenology at continental and global scales. In addition, the full-range (400-2500nm) hyperspectral measurements from the Hyperspectral Imager Suite (HISUI), and the Lidar data from the Global Ecosystem Dynamics Investigation (GEDI) onboard the International Space Station can also provide new insights into changes in leaf water content and biomass during the leaf senescence phase at the global scale (Stavros et al. 2017).

It is important to note that there is a wide variety of ecosystems within AHI's observation area ranging from drylands such as those in northwestern China and Australia to the tropical forests in Southeast Asia. Previous studies have demonstrated that it can be very challenging to have accurate LSP detections using satellite data in ecosystems such as drylands (Broich et al. 2014) and tropical forests (Guan et al. 2014; Yan et al. 2016b). Since we only focused on six sites in the temperate ecosystems of central and northern Japan, the evaluation results presented in this paper cannot provide a comprehensive picture of the applicability of AHI data in LSP detections, which needs to be examined using reference data (e.g., *in situ* phenological observations or time-lapse images from ground observation networks) from diverse types of ecosystems in future studies.

**Acknowledgment**

This work was supported by the NOAA GOES-R Risk Reduction Project GOES-R3#250, the NOAA contract JPSS_PGRR2_14, NASA contracts NNX15AB96A and 80NSSC18K0626, and the Global Change Observation Mission (PI #102 and 116) of Japan Aerospace Exploration Agency (JAXA).

## References


Cao, C., Luccia, F.J.D., Xiong, X., Wolfe, R., & Weng, F. (2014). Early On-Orbit Performance of the Visible Infrared Imaging Radiometer Suite Onboard the Suomi National Polar-Orbiting Partnership (S-NPP) Satellite. *IEEE Transactions on Geoscience and Remote Sensing, 52*, 1142-1156, doi: 10.1109/TGRS.2013.2247768.

Chen, J., Jönsson, P., Tamura, M., Gu, Z., Matsushita, B., & Eklundh, L. (2004). A simple method for reconstructing a high-quality NDVI time-series data set based on the Savitzky–Golay filter. *Remote Sensing of Environment, 91*, 332-344, doi: 10.1016/j.rse.2004.03.014.

Filippa, G., Cremonese, E., Migliavacca, M., Galvagno, M., Forkel, M., Wingate, L., Tomelleri, E., Morra di Cella, U., & Richardson, A.D. (2016). Phenopix: A R package for image-based vegetation phenology. *Agricultural and Forest Meteorology, 220*, 141-150, doi: 10.1016/j.agrformet.2016.01.006.

Friedl, M.A., Sulla-Menashe, D., Tan, B., Schneider, A., Ramankutty, N., Sibley, A., & Huang, X. (2010). MODIS Collection 5 global land cover: Algorithm refinements and characterization of new datasets. *Remote Sensing of Environment, 114*, 168-182, doi: 10.1016/j.rse.2009.08.016.

Jiang, Z., Huete, A.R., Didan, K., & Miura, T. (2008). Development of a two-band enhanced vegetation index without a blue band. *Remote Sensing of Environment, 112*, 3833-3845, doi: 10.1016/j.rse.2008.06.006.

Liu, H.Q., & Huete, A.R. (1995). A feedback based modification of the NDVI to minimize canopy background and atmospheric noise. *IEEE Transactions on Geoscience and Remote Sensing, 33*, 457-465.

Liu, L., Zhang, X., Yu, Y., & Guo, W. (2017). Real-time and short-term predictions of spring phenology in North America from VIIRS data. *Remote Sensing of Environment, 194*, 89-99, doi: 10.1016/j.rse.2017.03.009.

Nagai, S., Nasahara, K.N., Inoue, T., Saitoh, T.M., & Suzuki, R. (2016). Review: advances in in situ and satellite phenological observations in Japan. *International Journal of Biometeorology, 60*, 615-627, doi: 10.1007/s00484-015-1053-3.

Nasahara, K.N., & Nagai, S. (2015). Review: Development of an in situ observation network for terrestrial ecological remote sensing: the Phenological Eyes Network (PEN). *Ecological Research, 30*, 211-223, doi: 10.1007/s11284-014-1239-x.

Sonnentag, O., Hufkens, K., Teshera-Sterne, C., Young, A.M., Friedl, M., Braswell, B.H., Milliman, T., O'Keefe, J., & Richardson, A.D. (2012). Digital repeat photography for phenological research in forest ecosystems. *Agricultural and Forest Meteorology, 152*, 159-177, doi: 10.1016/j.agrformet.2011.09.009.

Toomey, M., Friedl, M.A., Frolking, S., Hufkens, K., Klosterman, S., Sonnentag, O., Baldocchi, D.D., Bernacchi, C.J., Biraud, S.C., Bohrer, G., Brzostek, E., Burns, S.P., Coursolle, C., Hollinger, D.Y., Margolis, H.A., McCaughey, H., Monson, R.K., Munger, J.W., Pallardy, S., Phillips, R.P., Torn, M.S., Wharton, S., Zeri, M., & Richardson, A.D. (2015). Greenness indices from digital cameras predict the timing and seasonal dynamics of canopy-scale photosynthesis. *Ecological Applications, 25*, 99-115, doi: 10.1890/14-0005.1.

Yan, D., Zhang, X., Yu, Y., & Guo, W. (2016a). A Comparison of Tropical Rainforest Phenology Retrieved From Geostationary (SEVIRI) and Polar-Orbiting (MODIS) Sensors Across the Congo Basin. *IEEE Transactions on Geoscience and Remote Sensing, 54*, 4867-4881, doi: 10.1109/TGRS.2016.2552462.

Yan, D., Zhang, X., Yu, Y., Guo, W., & Hanan, N.P. (2016b). Characterizing land surface phenology and responses to rainfall in the Sahara Desert. *Journal of Geophysical Research: Biogeosciences, 121*, 2243-2260, doi: 10.1002/2016JG003441.

Yu, F., & Wu, X. (2016). Radiometric Inter-Calibration between Himawari-8 AHI and S-NPP VIIRS for the Solar Reflective Bands. *Remote Sensing, 8*, 165, doi: 10.3390/rs8030165.

Zhang, X. (2015). Reconstruction of a complete global time series of daily vegetation index trajectory from long-term AVHRR data. *Remote Sensing of Environment, 156*, 457-472, doi: 10.1016/j.rse.2014.10.012.

Zhang, X., Friedl, M.A., Schaaf, C.B., Strahler, A.H., Hodges, J.C.F., Gao, F., Reed, B.C., & Huete, A. (2003). Monitoring vegetation phenology using MODIS. *Remote Sensing of Environment, 84*, 471-475, doi: 10.1016/S0034-4257(02)00135-9.

Zhang, X., Wang, J., Gao, F., Liu, Y., Schaaf, C., Friedl, M., Yu, Y., Jayavelu, S., Gray, J., Liu, L., Yan, D., & Henebry, G.M. (2017). Exploration of scaling effects on coarse resolution land surface phenology. *Remote Sensing of Environment, 190*, 318-330, doi: 10.1016/j.rse.2017.01.001.

An, S., Zhang, X., Chen, X., Yan, D. & Henebry, G.M. (2018). An exploration of Terrain effects on land surface phenology across the Qinghai-Tibet Plateau using Landsat ETM+ and OLI data. *Remote Sens.*, 10.

de Beurs, K.M. & Henebry, G.M. (2005). Land surface phenology and temperature variation in the International Geosphere-Biosphere Program high-latitude transects. *Glob. Chang. Biol.*, 11, 779–790.

de Beurs, K.M. & Henebry, G.M. (2008). War, drought, and phenology: Changes in the land surface phenology of Afghanistan since 1982. *J. Land Use Sci.*, 3, 95–111.

Broich, M., Huete, A., Tulbure, M.G., Ma, X., Xin, Q., Paget, M., Davies, K. & Devadas, R. (2014). Land surface phenological response to decadal climate variability across Australia using satellite remote sensing. *Biogeosciences*, 11, 5181–5198.

Brown, T.B., Hultine, K.R., Steltzer, H., Denny, E.G., Denslow, M.W., Granados, J., Henderson, S., Moore, D., Nagai, S., SanClements, M., Sánchez-Azofeifa, A., Sonnentag, O., Tazik, D. & Richardson, A.D. (2016). Using phenocams to monitor our changing Earth: toward a global phenocam network. *Front. Ecol. Environ.*, 14, 84–93.

Buyantuyev, A. & Wu, J. (2012). Urbanization diversifies land surface phenology in arid environments: Interactions among vegetation, climatic variation, and land use pattern in the Phoenix metropolitan region, USA. *Landsc. Urban Plan.*, 105, 149–159.

Choi, Y.-Y. & Suh, M.-S. (2018). Development of Himawari-8/Advanced Himawari Imager (AHI) Land Surface Temperature Retrieval Algorithm. *Remote Sens.*, 10, 2013.

Delbart, N., Beaubien, E., Kergoat, L. & Le Toan, T. (2015). Comparing land surface phenology with leafing and flowering observations from the PlantWatch citizen network. *Remote Sens. Environ.*, 160, 273–280.

Elmore, A.J., Guinn, S.M., Minsley, B.J. & Richardson, A.D. (2012). Landscape controls on the timing of spring, autumn, and growing season length in mid-Atlantic forests. *Glob. Chang. Biol.*, 18, 656–674.

Fensholt, R., Ayamba, A.., Stisen, S.., Sandholt, I.., Pak, E.. & Small, J.. (2007). Comparisons of compositing period length for vegetation index data from polar-orbiting and geostationary satellites for the cloud-prone region of West Africa. *Photogramm. Eng. Remote Sensing*, 73, 297–309.

Ganguly, S., Friedl, M.A., Tan, B., Zhang, X. & Verma, M. (2010). Land surface phenology from MODIS: Characterization of the Collection 5 global land cover dynamics product. *Remote Sens.*

*Environ.*, 114, 1805–1816.

Gonsamo, A., Chen, J.M., Price, D.T., Kurz, W.A. & Wu, C. (2012). Land surface phenology from optical satellite measurement and CO2 eddy covariance technique. *J. Geophys. Res. Biogeosciences*, 117, n/a-n/a.

Guan, K., Medvigy, D., Wood, E.F., Caylor, K.K., Li, S. & Jeong, S.J. (2014). Deriving vegetation phenological time and trajectory information over africa using seviri daily LAI. *IEEE Trans. Geosci. Remote Sens.*, 52, 1113–1130.

Hashimoto, S., Tadono, T., Onosato, M., Hori, M. & Shiomi, K. (2014). A New Method to Derive Precise Land-use and Land-cover Maps Using Multi-temporal Optical Data. *J. Remote Sens. Soc. Japan*, 34, 102–112.

Huete, A., Didan, K., Miura, T., Rodriguez, E.P., Gao, X. & Ferreira, L.G. (2002). Overview of the radiometric and biophysical performance of the MODIS vegetation indices. *Remote Sens. Environ.*, 83, 195–213.

Hufkens, K., Friedl, M., Sonnentag, O., Braswell, B.H., Milliman, T. & Richardson, A.D. (2012). Linking near-surface and satellite remote sensing measurements of deciduous broadleaf forest phenology. *Remote Sens. Environ.*, 117, 307–321.

Jiang, Z., Huete, A.R., Didan, K. & Miura, T. (2008). Development of a two-band enhanced vegetation index without a blue band. *Remote Sens. Environ.*, 112, 3833–3845.

Keenan, T.F., Darby, B., Felts, E., Sonnentag, O., Friedl, M.A., Hufkens, K., O'Keefe, J., Klosterman, S., Munger, J.W., Toomey, M. & Richardson, A.D. (2014). Tracking forest phenology and seasonal physiology using digital repeat photography: a critical assessment. *Ecol. Appl.*, 24, 1478–1489.

Klosterman, S.T., Hufkens, K., Gray, J.M., Melaas, E., Sonnentag, O., Lavine, I., Mitchell, L., Norman, R., Friedl, M.A. & Richardson, A.D. (2014). Evaluating remote sensing of deciduous forest phenology at multiple spatial scales using PhenoCam imagery. *Biogeosciences*, 11, 4305–4320.

Kobayashi, H., Nagai, S., Kim, Y., Yang, W., Ikeda, K., Ikawa, H., Nagano, H. & Suzuki, R. (2018). In situ observations reveal how spectral reflectance responds to growing season phenology of an open evergreen forest in Alaska. *Remote Sens.*, 10.

Köehler, P., Frankenberg, C., Magney, T.S., Guanter, L., Joiner, J. & Landgraf, J. (2018). Global retrievals of solar induced chlorophyll fluorescence with TROPOMI: first results and inter-sensor comparison to OCO-2. *Geophys. Res. Lett.*, Accepted.

Krehbiel, C., Zhang, X. & Henebry, G.M. (2017). Impacts of thermal time on land surface phenology in urban areas. *Remote Sens.*, 9, 1–21.

Liang, L., Schwartz, M.D. & Fei, S. (2011). Validating satellite phenology through intensive ground observation and landscape scaling in a mixed seasonal forest. *Remote Sens. Environ.*, 115, 143–157.

Liu, Y., Hill, M.J., Zhang, X., Wang, Z., Richardson, A.D., Hufkens, K., Filippa, G., Baldocchi, D.D., Ma, S., Verfaillie, J. & Schaaf, C.B. (2017). Using data from Landsat, MODIS, VIIRS and PhenoCams to monitor the phenology of California oak/grass savanna and open grassland across spatial scales. *Agric. For. Meteorol.*, 237–238, 311–325.

Lu, X., Liu, Z., Zhou, Y., Liu, Y., An, S. & Tang, J. (2018). Comparison of phenology estimated from reflectance-based indices and solar-induced chlorophyll fluorescence (SIF) observations in a temperate forest using GPP-based phenology as the standard. *Remote Sens.*, 10.

Melaas, E.K., Sulla-Menashe, D., Gray, J.M., Black, T.A., Morin, T.H., Richardson, A.D. & Friedl, M.A. (2016). Multisite analysis of land surface phenology in North American temperate and boreal deciduous forests from Landsat. *Remote Sens. Environ.*, 186, 452–464.

Moore, N., Crowell, S., Rayner, P., Kumer, J., O'Dell, C., O'Brien, D., Utembe, S., Polonsky, I., Schimel, D. & Lemen, J. (2018). The Potential of the Geostationary Carbon Cycle Observatory (GeoCarb) to Provide Multi-scale Constraints on the Carbon Cycle in the Americas. *Front. Environ. Sci.*, 6, 1–13.

Motohka, T., Nasahara, K.N., Miyata, A., Mano, M. & Tsuchida, S. (2009). Evaluation of optical satellite remote sensing for rice paddy phenology in monsoon Asia using a continuous in situ dataset. *Int. J. Remote Sens.*, 30, 4343–4357.

Nagai, S., Akitsu, T., Saitoh, T.M., Busey, R.C., Fukuzawa, K., Honda, Y., Ichie, T., Ide, R., Ikawa, H., Iwasaki, A., Iwao, K., Kajiwara, K., Kang, S., Kim, Y., Khoon, K.L., Kononov, A. V., Kosugi, Y., Maeda, T., Mamiya, W., Matsuoka, M., Maximov, T.C., Menzel, A., Miura, T., Mizunuma, T., Morozumi, T., Motohka, T., Muraoka, H., Nagano, H., Nakai, T., Nakaji, T., Oguma, H., Ohta, T., Ono, K., Pungga, R.A.S., Petrov, R.E., Sakai, R., Schunk, C., Sekikawa, S., Shakhmatov, R., Son, Y., Sugimoto, A., Suzuki, R., Takagi, K., Takanashi, S., Tei, S., Tsuchida, S., Yamamoto, H., Yamasaki, E., Yamashita, M., Yoon, T.K., Yoshida, T., Yoshimura, M., Yoshitake, S., Wilkinson, M., Wingate, L. & Nasahara, K.N. (2018). 8 million phenological and sky images from 29 ecosystems from the Arctic to the tropics: the Phenological Eyes Network. *Ecol. Res.*, 1–2.

Nagai, S., Ichie, T., Yoneyama, A., Kobayashi, H., Inoue, T., Ishii, R., Suzuki, R. & Itioka, T. (2016a). Usability of time-lapse digital camera images to detect characteristics of tree phenology in a tropical rainforest. *Ecol. Inform.*, 32, 91–106.

Nagai, S., Nasahara, K.N., Inoue, T., Saitoh, T.M. & Suzuki, R. (2016b). Review: advances in in situ and satellite phenological observations in Japan. *Int. J. Biometeorol.*, 60, 615–627.

Nagai, S., Saigusa, N., Muraoka, H. & Nasahara, K.N. (2010). What makes the satellite-based EVI-GPP relationship unclear in a deciduous broad-leaved forest? *Ecol. Res.*, 25, 359–365.

Nagai, S., Saitoh, T.M., Noh, N.J., Yoon, T.K., Kobayashi, H., Suzuki, R., Nasahara, K.N., Son, Y. & Muraoka, H. (2013). Utility of information in photographs taken upwards from the floor of closed-canopy deciduous broadleaved and closed-canopy evergreen coniferous forests for continuous observation of canopy phenology. *Ecol. Inform.*, 18, 10–19.

Nasahara, K.N. & Nagai, S. (2015). Review: Development of an in situ observation network for terrestrial ecological remote sensing: the Phenological Eyes Network (PEN). *Ecol. Res.*, 30, 211–223.

ORNL-DAAC. (2018). MODIS and VIIRS Land Products Global Subsetting and Visualization Tool.

Peng, D., Wu, C., Li, C., Zhang, X., Liu, Z., Ye, H., Luo, S., Liu, X., Hu, Y. & Fang, B. (2017). Spring green-up phenology products derived from MODIS NDVI and EVI: Intercomparison, interpretation and validation using National Phenology Network and AmeriFlux observations. *Ecol. Indic.*, 77, 323–336.

Richardson, A.D., Hufkens, K., Milliman, T., Aubrecht, D.M., Chen, M., Gray, J.M., Johnston, M.R., Keenan, T.F., Klosterman, S.T., Kosmala, M., Melaas, E.K., Friedl, M.A. & Frolking, S. (2018a). Tracking vegetation phenology across diverse North American biomes using PhenoCam imagery. *Sci. Data*, 5, 180028.

Richardson, A.D., Hufkens, K., Milliman, T. & Frolking, S. (2018b). Intercomparison of phenological transition dates derived from the PhenoCam Dataset V1.0 and MODIS satellite remote sensing. *Sci. Rep.*, 8, 5679.

Richardson, A.D., Keenan, T.F., Migliavacca, M., Ryu, Y., Sonnentag, O. & Toomey, M. (2013). Climate change, phenology, and phenological control of vegetation feedbacks to the climate system. *Agric. For. Meteorol.*, 169, 156–173.

Riggs, G.A., Hall, D.K. & Salomonson, V. V. (1994). A snow index for the Landsat Thematic Mapper and Moderate Resolution Imaging Spectroradiometer. In: *Proc. IGARSS '94 - 1994 IEEE Int. Geosci. Remote Sens. Symp.* pp. 1942–1944 vol.4.

Rodriguez-Galiano, V.F., Dash, J. & Atkinson, P.M. (2015). Intercomparison of satellite sensor land surface phenology and ground phenology in Europe. *Geophys. Res. Lett.*, 42, 2253–2260.

Sakamoto, T., Van Nguyen, N., Ohno, H., Ishitsuka, N. & Yokozawa, M. (2006). Spatio-temporal distribution of rice phenology and cropping systems in the Mekong Delta with special reference to the seasonal water flow of the Mekong and Bassac rivers. *Remote Sens. Environ.*, 100, 1–16.

Sakamoto, T., Wardlow, B.D., Gitelson, A.A., Verma, S.B., Suyker, A.E. & Arkebauer, T.J. (2010). A Two-Step Filtering approach for detecting maize and soybean phenology with time-series MODIS data. *Remote Sens. Environ.*, 114, 2146–2159.

Sobrino, J.A., Julien, Y. & Soria, G. (2013). Phenology estimation from meteosat second generation data. *IEEE J. Sel. Top. Appl. Earth Obs. Remote Sens.*, 6, 1653–1659.

Sonnentag, O., Hufkens, K., Teshera-Sterne, C., Young, A.M., Friedl, M., Braswell, B.H., Milliman, T., O'Keefe, J. & Richardson, A.D. (2012). Digital repeat photography for phenological research in forest ecosystems. *Agric. For. Meteorol.*, 152, 159–177.

Soudani, K., le Maire, G., Dufrêne, E., François, C., Delpierre, N., Ulrich, E. & Cecchini, S. (2008). Evaluation of the onset of green-up in temperate deciduous broadleaf forests derived from Moderate Resolution Imaging Spectroradiometer (MODIS) data. *Remote Sens. Environ.*, 112, 2643–2655.

Stavros, E.N., Schimel, D., Pavlick, R., Serbin, S., Swann, A., Duncanson, L., Fisher, J.B., Fassnacht, F., Ustin, S., Dubayah, R., Schweiger, A. & Wennberg, P. (2017). ISS observations offer insights into plant function. *Nat. Ecol. Evol.*, 1, 1–4.

Suepa, T., Qi, J., Lawawirojwong, S. & Messina, J.P. (2016). Understanding spatio-temporal variation of vegetation phenology and rainfall seasonality in the monsoon Southeast Asia. *Environ. Res.*, 147, 621–629.

Tian, Y., Romanov, P., Yu, Y., Xu, H. & Tarpley, D. (2010). Analysis of vegetation index NDVI anisotropy to improve the accuracy of the GOES-R Green Vegetation Fraction product. *Int. Geosci. Remote Sens. Symp.*, 2091–2094.

Walker, J.J., de Beurs, K.M. & Henebry, G.M. (2015). Land surface phenology along urban to rural gradients in the U.S. Great Plains. *Remote Sens. Environ.*, 165, 42–52.

Xie, J., Kneubühler, M., Garonna, I., Notarnicola, C., De Gregorio, L., De Jong, R., Chimani, B. & Schaepman, M.E. (2017). Altitude-dependent influence of snow cover on alpine land surface phenology. *J. Geophys. Res. Biogeosciences*, 122, 1107–1122.

Yan, D., Zhang, X., Yu, Y. & Guo, W. (2016a). A Comparison of Tropical Rainforest Phenology Retrieved From Geostationary (SEVIRI) and Polar-Orbiting (MODIS) Sensors Across the Congo Basin. *IEEE Trans. Geosci. Remote Sens.*

Yan, D., Zhang, X., Yu, Y. & Guo, W. (2016b). A Comparison of Tropical Rainforest Phenology Retrieved from Geostationary (SEVIRI) and Polar-Orbiting (MODIS) Sensors Across the Congo Basin. *IEEE Trans. Geosci. Remote Sens.*, 54, 4867–4881.

Zhang, X. (2015). Reconstruction of a complete global time series of daily vegetation index trajectory from long-term AVHRR data. *Remote Sens. Environ.*, 156, 457–472.

Zhang, X., Friedl, M.A. & Schaaf, C.B. (2006). Global vegetation phenology from Moderate Resolution Imaging Spectroradiometer (MODIS): Evaluation of global patterns and comparison with in situ measurements. *J. Geophys. Res.*, 111, G04017.

Zhang, X., Friedl, M.A. & Schaaf, C.B. (2009). Sensitivity of vegetation phenology detection to the temporal resolution of satellite data. *Int. J. Remote Sens.*, 30, 2061–2074.

Zhang, X., Friedl, M.A., Schaaf, C.B. & Strahler, A.H. (2004a). Climate controls on vegetation phenological patterns in northern mid- and high latitudes inferred from MODIS data. *Glob. Chang. Biol.*, 10, 1133–1145.

Zhang, X., Friedl, M.A., Schaaf, C.B., Strahler, A.H., Hodges, J.C.F., Gao, F., Reed, B.C. & Huete, A. (2003). Monitoring vegetation phenology using MODIS. *Remote Sens. Environ.*, 84, 471–475.

Zhang, X., Friedl, M.A., Schaaf, C.B., Strahler, A.H. & Schneider, A. (2004b). The footprint of urban climates on vegetation phenology. *Geophys. Res. Lett.*, 31, 10–13.

Zhang, X., Jayavelu, S., Liu, L., Friedl, M.A., Henebry, G.M., Liu, Y., Schaaf, C.B., Richardson, A.D. & Gray, J. (2018a). Evaluation of land surface phenology from VIIRS data using time series of PhenoCam imagery. *Agric. For. Meteorol.*, 256–257, 137–149.

Zhang, X., Liu, L., Liu, Y., Jayavelu, S., Wang, J., Moon, M., Henebry, G.M., Friedl, M.A. & Schaaf, C.B. (2018b). Generation and evaluation of the VIIRS land surface phenology product. *Remote Sens. Environ.*, 216, 212–229.

Zhang, X., Liu, L. & Yan, D. (2017). Comparisons of global land surface seasonality and phenology derived from AVHRR, MODIS, and VIIRS data. *J. Geophys. Res. Biogeosciences*, 122, 1506–1525.

de Beurs, K.M. & Henebry, G.M. (2008). War, drought, and phenology: changes in the land surface phenology of Afghanistan since 1982. *J. Land Use Sci.*, 3, 95–111.

Brown, T.B., Hultine, K.R., Steltzer, H., Denny, E.G., Denslow, M.W., Granados, J., Henderson, S., Moore, D., Nagai, S., SanClements, M., Sánchez-Azofeifa, A., Sonnentag, O., Tazik, D. & Richardson, A.D. (2016). Using phenocams to monitor our changing Earth: toward a global phenocam network. *Front. Ecol. Environ.*, 14, 84–93.

D'Odorico, P., Gonsamo, A., Gough, C.M., Bohrer, G., Morison, J., Wilkinson, M., Hanson, P.J., Gianelle, D., Fuentes, J.D. & Buchmann, N. (2015). The match and mismatch between photosynthesis and land surface phenology of deciduous forests. *Agric. For. Meteorol.*, 214–215, 25–38.

Elmendorf, S.C., Jones, K.D., Cook, B.I., Diez, J.M., Enquist, C.A.F., Hufft, R.A., Jones, M.O., Mazer, S.J., Miller-Rushing, A.J., Moore, D.J.P., Schwartz, M.D. & Weltzin, J.F. (2016). The plant phenology monitoring design for The National Ecological Observatory Network. *Ecosphere*, 7, e01303–n/a.

Elmore, A.J., Guinn, S.M., Minsley, B.J. & Richardson, A.D. (2012). Landscape controls on the timing of spring, autumn, and growing season length in mid-Atlantic forests. *Glob. Chang. Biol.*, 18, 656–674.

Elmore, J.A., Stylinski, D.C. & Pradhan, K. (2016). Synergistic Use of Citizen Science and Remote Sensing for Continental-Scale Measurements of Forest Tree Phenology. *Remote Sens.* .

Ganguly, S., Friedl, M.A., Tan, B., Zhang, X. & Verma, M. (2010). Land surface phenology from

MODIS: Characterization of the Collection 5 global land cover dynamics product. *Remote Sens. Environ.*, 114, 1805–1816.

Gonsamo, A., Chen, J.M., Price, D.T., Kurz, W.A. & Wu, C. (2012). Land surface phenology from optical satellite measurement and CO2 eddy covariance technique. *J. Geophys. Res. Biogeosciences*, 117, n/a-n/a.

Guan, K., Medvigy, D., Wood, E.F., Caylor, K.K., Li, S. & Jeong, S.J. (2014). Deriving Vegetation Phenological Time and Trajectory Information Over Africa Using SEVIRI Daily LAI. *IEEE Trans. Geosci. Remote Sens.*

Hmimina, G., Dufrêne, E., Pontailler, J.-Y., Delpierre, N., Aubinet, M., Caquet, B., de Grandcourt, A., Burban, B., Flechard, C., Granier, A., Gross, P., Heinesch, B., Longdoz, B., Moureaux, C., Ourcival, J.-M., Rambal, S., Saint André, L. & Soudani, K. (2013). Evaluation of the potential of MODIS satellite data to predict vegetation phenology in different biomes: An investigation using ground-based NDVI measurements. *Remote Sens. Environ.*, 132, 145–158.

Hufkens, K., Friedl, M., Sonnentag, O., Braswell, B.H., Milliman, T. & Richardson, A.D. (2012). Linking near-surface and satellite remote sensing measurements of deciduous broadleaf forest phenology. *Remote Sens. Environ.*, 117, 307–321.

Keenan, T.F., Darby, B., Felts, E., Sonnentag, O., Friedl, M.A., Hufkens, K., O'Keefe, J., Klosterman, S., Munger, J.W., Toomey, M. & Richardson, A.D. (2014). Tracking forest phenology and seasonal physiology using digital repeat photography: a critical assessment. *Ecol. Appl.*, 24, 1478–1489.

Liu, L., Liang, L., Schwartz, M.D., Donnelly, A., Wang, Z., Schaaf, C.B. & Liu, L. (2015). Evaluating the potential of MODIS satellite data to track temporal dynamics of autumn phenology in a temperate mixed forest. *Remote Sens. Environ.*, 160, 156–165.

Liu, Y., Hill, M.J., Zhang, X., Wang, Z., Richardson, A.D., Hufkens, K., Filippa, G., Baldocchi, D.D., Ma, S., Verfaillie, J. & Schaaf, C.B. (2017). Using data from Landsat, MODIS, VIIRS and PhenoCams to monitor the phenology of California oak/grass savanna and open grassland across spatial scales. *Agric. For. Meteorol.*, 237–238, 311–325.

McKinley, D.C., Miller-Rushing, A.J., Ballard, H.L., Bonney, R., Brown, H., Cook-Patton, S.C., Evans, D.M., French, R.A., Parrish, J.K., Phillips, T.B., Ryan, S.F., Shanley, L.A., Shirk, J.L., Stepenuck, K.F., Weltzin, J.F., Wiggins, A., Boyle, O.D., Briggs, R.D., Chapin, S.F., Hewitt, D.A., Preuss, P.W. & Soukup, M.A. (2017). Citizen science can improve conservation science, natural resource management, and environmental protection. *Biol. Conserv.*, 208, 15–28.

Melaas, E.K., Sulla-Menashe, D., Gray, J.M., Black, T.A., Morin, T.H., Richardson, A.D. & Friedl, M.A. (2016). Multisite analysis of land surface phenology in North American temperate and boreal deciduous forests from Landsat. *Remote Sens. Environ.*, 186, 452–464.

Nagai, S., Nasahara, K.N., Inoue, T., Saitoh, T.M. & Suzuki, R. (2016). Review: advances in in situ and satellite phenological observations in Japan. *Int. J. Biometeorol.*, 60, 615–627.

Nasahara, K.N. & Nagai, S. (2015). Review: Development of an in situ observation network for terrestrial ecological remote sensing: the Phenological Eyes Network (PEN). *Ecol. Res.*, 30, 211–223.

Peng, D., Wu, C., Li, C., Zhang, X., Liu, Z., Ye, H., Luo, S., Liu, X., Hu, Y. & Fang, B. (2017a). Spring green-up phenology products derived from MODIS NDVI and EVI: Intercomparison, interpretation and validation using National Phenology Network and AmeriFlux observations. *Ecol. Indic.*, 77, 323–336.

Peng, D., Zhang, X., Wu, C., Huang, W., Gonsamo, A., Huete, A.R., Didan, K., Tan, B., Liu, X. & Zhang,

B. (2017b). Intercomparison and evaluation of spring phenology products using National Phenology Network and AmeriFlux observations in the contiguous United States. *Agric. For. Meteorol.*, 242, 33–46.

Petach, A.R., Toomey, M., Aubrecht, D.M. & Richardson, A.D. (2014). Monitoring vegetation phenology using an infrared-enabled security camera. *Agric. For. Meteorol.*, 195, 143–151.

Richardson, A.D., Braswell, B.H., Hollinger, D.Y., Jenkins, J.P. & Ollinger, S. V. (2009). Near-surface remote sensing of spatial and temporal variation in canopy phenology. *Ecol. Appl.*, 19, 1417–1428.

Rodriguez-Galiano, V.F., Dash, J. & Atkinson, P.M. (2015). Intercomparison of satellite sensor land surface phenology and ground phenology in Europe. *Geophys. Res. Lett.*, 42, 2253–2260.

Tian, Y., Romanov, P., Yu, Y., Xu, H. & Tarpley, D. (2010). Analysis of vegetation index NDVI anisotropy to improve the accuracy of the GOES-R Green Vegetation Fraction product. *Int. Geosci. Remote Sens. Symp.*, 2091–2094.

Yan, D., Zhang, X., Yu, Y. & Guo, W. (2016). A Comparison of Tropical Rainforest Phenology Retrieved From Geostationary (SEVIRI) and Polar-Orbiting (MODIS) Sensors Across the Congo Basin. *IEEE Trans. Geosci. Remote Sens.*

Zhang, X. (2015). Reconstruction of a complete global time series of daily vegetation index trajectory from long-term AVHRR data. *Remote Sens. Environ.*, 156, 457–472.

Zhang, X., Friedl, M.A., Schaaf, C.B., Strahler, A.H., Hodges, J.C.F., Gao, F., Reed, B.C. & Huete, A. (2003). Monitoring vegetation phenology using MODIS. *Remote Sens. Environ.*, 84, 471–475.

Zhang, X., Friedl, M.A., Schaaf, C.B., Strahler, A.H. & Schneider, A. (2004). The footprint of urban climates on vegetation phenology. *Geophys. Res. Lett.*, 31, 10–13.

Zhang, X., Liu, L. & Yan, D. (2017). Comparisons of global land surface seasonality and phenology derived from AVHRR, MODIS, and VIIRS data. *J. Geophys. Res. Biogeosciences*, 122, 1506–1525.

# Supplemental information for "Evaluating land surface phenology retrieved from the Advanced Himawari Imager using in-situ observations from the Phenological Eyes Network"

**Contents of this file:**

Supplementary tables S1-S6

Supplementary figures S1 – S6

**Supplementary table**

Table S1. Geographic coordinate and land cover of the study sites.

| Site | Latitude/Longitude | Land cover |
|---|---|---|
| Fuji-Hokuroku (FHK) | 35.44°N / 138.76°E | Deciduous needleleaf forest |
| Mase flux site (MSE) | 36.05°N / 140.03°E | Rice paddy |
| Mt. Tsukuba (MTK) | 36.23°N / 140.10°E | Mixed forest |
| TERC grass field (TGF) | 36.11°N / 140.10°E | Grass |
| Takayama flux site (TKY) | 36.14°N / 137.42°E | Deciduous broadleaf forest |
| Teshio CC-LaG site (TSE) | 45.01°N / 142.11°E | Deciduous needle-leaf plantation and dwarf bamboo |

Table S2. The standard deviation in the detected SOS across latitudinal and elevation gradients

| | High Latitude: 42°N – 45.5°N | | | | | |
|---|---|---|---|---|---|---|
| Elevation (m) | Urban | Rice paddy | Non-rice crop | Grass | Deciduous forest | Evergreen forest |
| 0 - 200 | 13 | 14 | 9 | 8 | 8 | 8 |
| 200 - 500 | 8 | 9 | 8 | 8 | 7 | 7 |
| 500 – 3100 | 8 | 5 | 6 | 11 | 8 | 8 |
| | Medium Latitude: 38.5°N – 42°N | | | | | |
| 0 - 200 | 28 | 30 | 24 | 18 | 15 | 19 |
| 200 - 500 | 18 | 14 | 14 | 14 | 12 | 17 |
| 500 – 3100 | | 5 | 11 | 8 | 7 | 13 |
| | Low Latitude: 35°N – 38.5°N | | | | | |
| 0 - 200 | 31 | 30 | 24 | 21 | 17 | 19 |
| 200 - 500 | 23 | 21 | 19 | 16 | 14 | 19 |
| 500 – 3100 | 20 | 18 | 17 | 12 | 13 | 19 |

Table S3. The standard deviation in the detected EOS across latitudinal and elevation gradients

| | High Latitude: 42°N – 45.5°N | | | | | |
|---|---|---|---|---|---|---|
| Elevation (m) | Urban | Rice paddy | Non-rice crop | Grass | Deciduous forest | Evergreen forest |
| 0 - 200 | 20 | 20 | 15 | 11 | 9 | 10 |
| 200 - 500 | 17 | 17 | 11 | 8 | 8 | 7 |
| 500 – 3100 | 8 | 9 | 4 | 11 | 9 | 10 |
| | Medium Latitude: 38.5°N – 42°N | | | | | |
| 0 - 200 | 25 | 16 | 24 | 23 | 23 | 25 |
| 200 - 500 | 20 | 21 | 20 | 14 | 12 | 18 |
| 500 – 3100 | | 1 | 10 | 15 | 7 | 8 |
| | Low Latitude: 35°N – 38.5°N | | | | | |
| 0 - 200 | 27 | 22 | 23 | 26 | 24 | 27 |
| 200 - 500 | 27 | 28 | 26 | 21 | 20 | 34 |
| 500 – 3100 | 26 | 29 | 26 | 17 | 17 | 34 |

Table S4. The standard deviation in the detected SOF across latitudinal and elevation gradients

| | High Latitude: 42°N – 45.5°N | | | | | |
|---|---|---|---|---|---|---|
| Elevation (m) | Urban | Rice paddy | Non-rice crop | Grass | Deciduous forest | Evergreen forest |
| 0 - 200 | 20 | 10 | 11 | 15 | 13 | 17 |
| 200 - 500 | 10 | 8 | 12 | 14 | 11 | 13 |
| 500 – 3100 | 11 | 6 | 8 | 14 | 12 | 14 |
| | Medium Latitude: 38.5°N – 42°N | | | | | |
| 0 - 200 | 20 | 14 | 16 | 16 | 16 | 18 |
| 200 - 500 | 12 | 15 | 13 | 13 | 14 | 17 |
| 500 – 3100 | | 9 | 12 | 12 | 12 | 13 |
| | Low Latitude: 35°N – 38.5°N | | | | | |
| 0 - 200 | 24 | 17 | 20 | 19 | 20 | 22 |
| 200 - 500 | 22 | 20 | 19 | 15 | 19 | 23 |
| 500 – 3100 | 16 | 20 | 17 | 15 | 17 | 22 |

Table S5. The standard deviation in the detected EOF across latitudinal and elevation gradients

| | High Latitude: 42°N – 45.5°N | | | | | |
|---|---|---|---|---|---|---|
| Elevation (m) | Urban | Rice paddy | Non-rice crop | Grass | Deciduous forest | Evergreen forest |
| 0 - 200 | 20 | 17 | 17 | 33 | 23 | 27 |
| 200 - 500 | 16 | 7 | 12 | 18 | 14 | 15 |
| 500 – 3100 | 8 | 4 | 5 | 15 | 12 | 14 |
| | Medium Latitude: 38.5°N – 42°N | | | | | |
| 0 - 200 | 27 | 22 | 23 | 18 | 17 | 17 |
| 200 - 500 | 14 | 11 | 10 | 10 | 10 | 11 |
| 500 – 3100 | | 4 | 7 | 7 | 8 | 9 |
| | Low Latitude: 35°N – 38.5°N | | | | | |
| 0 - 200 | 47 | 34 | 34 | 30 | 21 | 25 |
| 200 - 500 | 27 | 21 | 20 | 16 | 14 | 24 |
| 500 – 3100 | 17 | 17 | 16 | 14 | 12 | 19 |

Table S6. Summary of the regression statistics.

| | x=PEN, y=AHI | | | | x=PEN, y=MODIS | | | | x=AHI, y=MODIS | | | |
|---|---|---|---|---|---|---|---|---|---|---|---|---|
| | $R^2$ | Intercept | Slope | *p* | $R^2$ | Intercept | Slope | *p* | $R^2$ | Intercept | Slope | *p* |
| **SOS** | 0.75 | -26.46 | 1.23 | <0.001 | 0.46 | -9.71 | 1.11 | <0.05 | 0.59 | 16.21 | 0.88 | <0.005 |
| **EOS** | 0.43 | 15.05 | 0.95 | <0.05 | 0.01 | 156.84 | 0.10 | >0.5 | 0.13 | 128.94 | 0.28 | >0.5 |
| **SOF** | 7E-8 | 243.10 | 5E-3 | >0.5 | 1E-3 | 146.99 | 0.42 | >0.5 | 4E-3 | 167.72 | 0.36 | >0.5 |
| **EOF** | 0.49 | 55.52 | 0.89 | <0.05 | 0.41 | -34.00 | 1.14 | <0.05 | 0.57 | -30.04 | 1.05 | <0.005 |

**Supplementary figures**

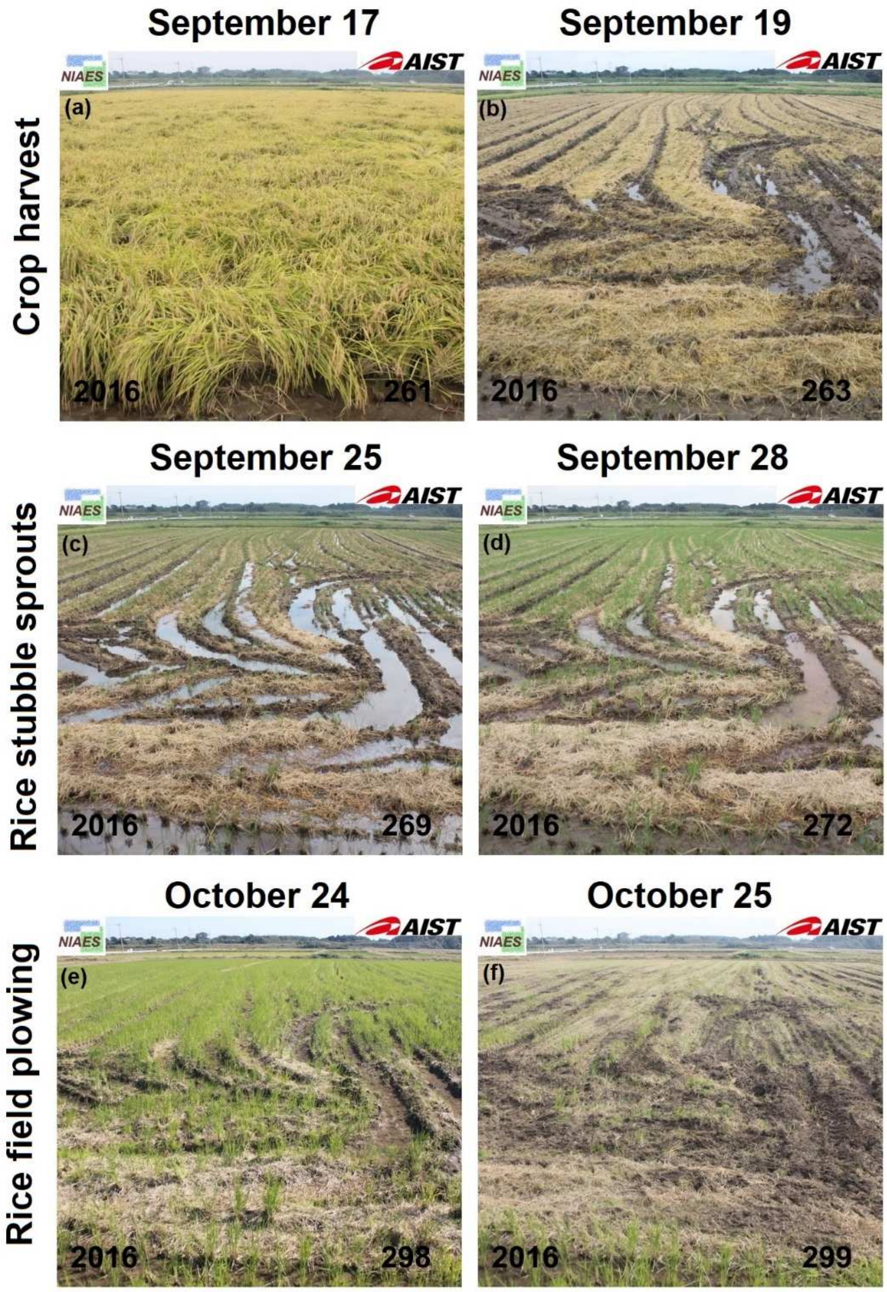


**Figure S1**. The abrupt changes in crop cover between September 17 and October 25, 2016 at the MSE site. The top, middle and bottom panels showing images of crop harvest, emergence of rice stubble sprouts and the removal of stubble sprouts by plowing, respectively.

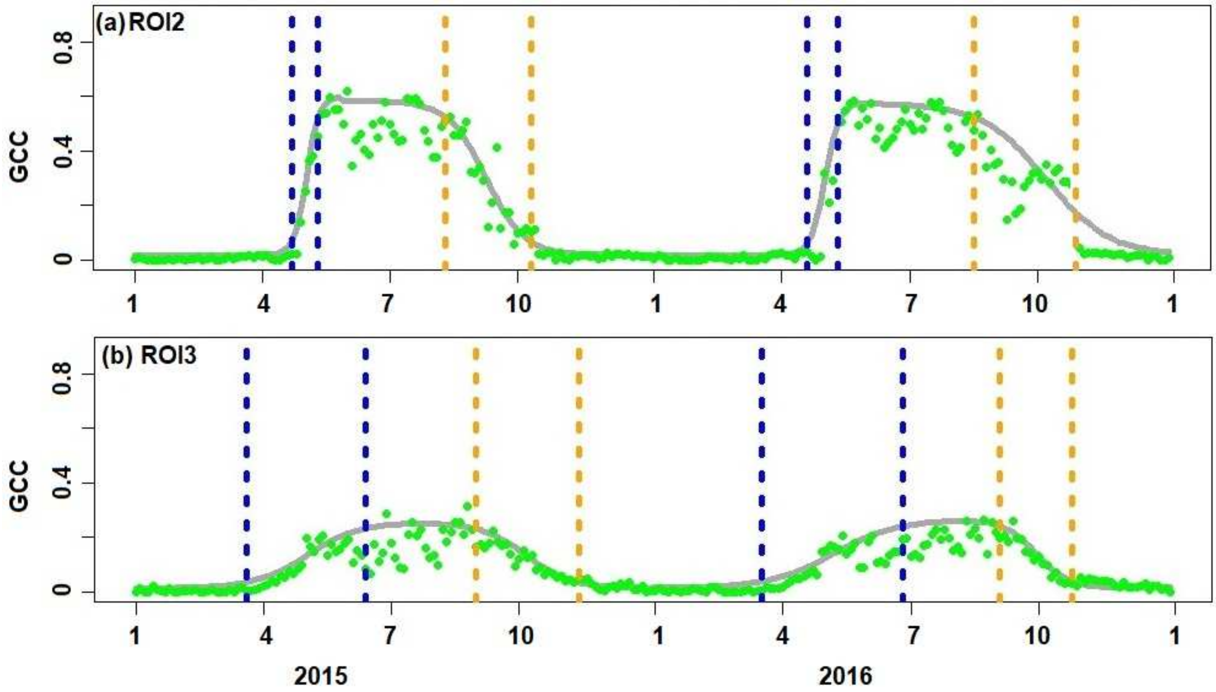


**Figure S2**. Phenological detection results for ROI2 and ROI3 at the MSE site. Solid green circles represent the original snow-free GCC, respectively. The grey solid lines represent the reconstructed greenness trajectories. The blue dashed lines represent the detected SOS and EOS whereas orange dashed lines represent SOF and EOF.

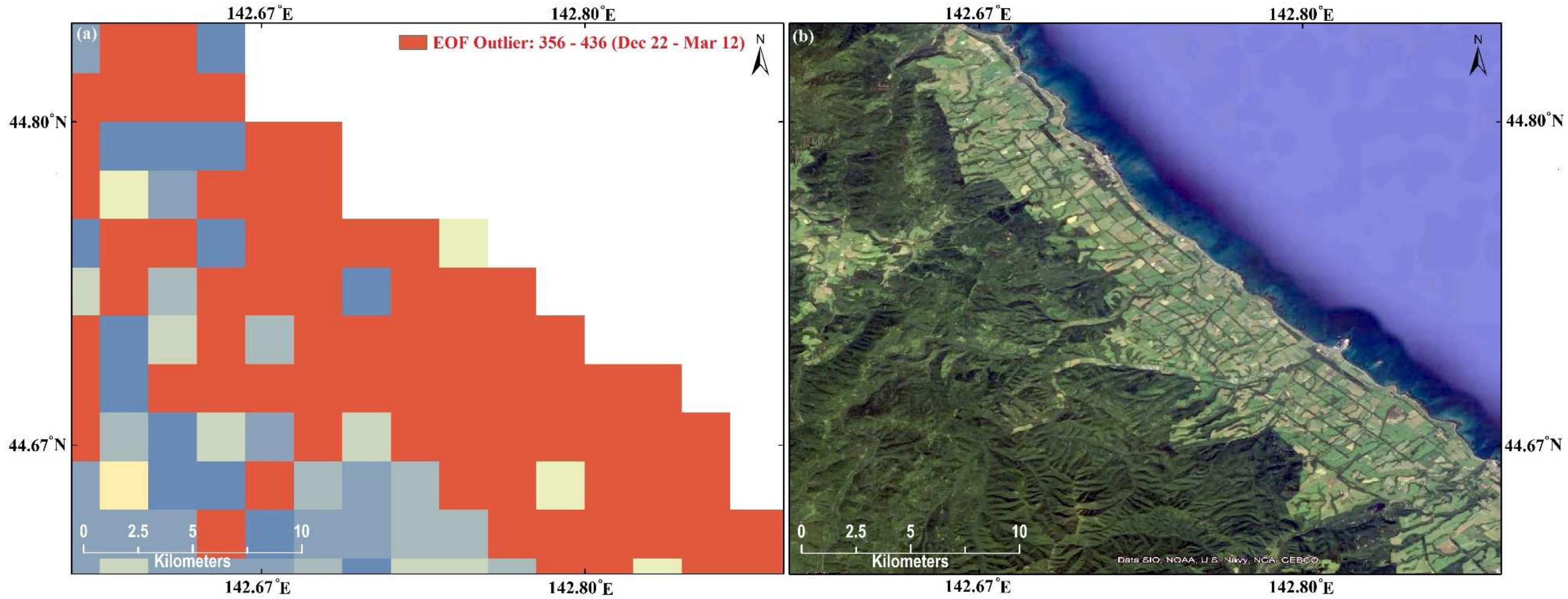


**Figure S3**. The spatial pattern of EOF outliers (a) and a high-resolution Google Earth image (b) in the coastal areas of northern Japan. The acquisition date of the Google Earth image is 12/30/2016.

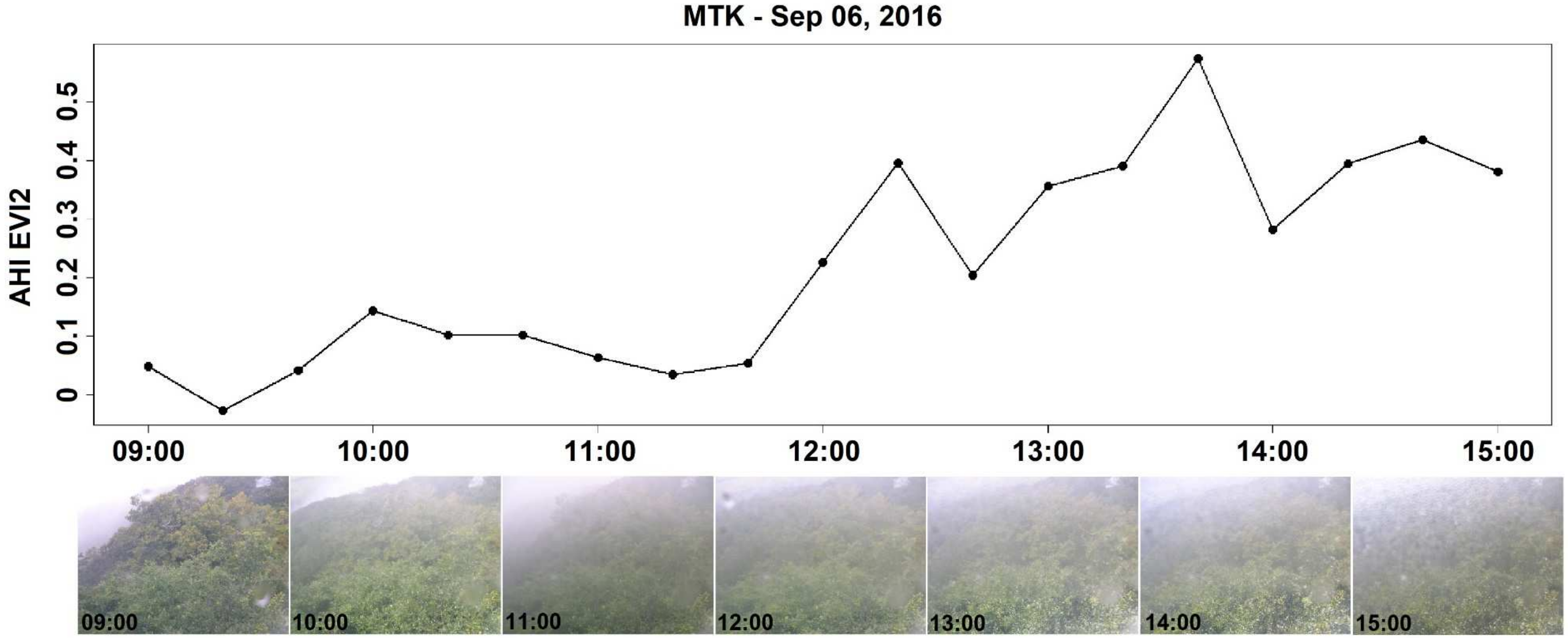


**Figure S4**. The 20min EVI2 (top row) and hourly photographs (bottom row) between 09:00 and 15:00 at the MTK site on September 06, 2016.

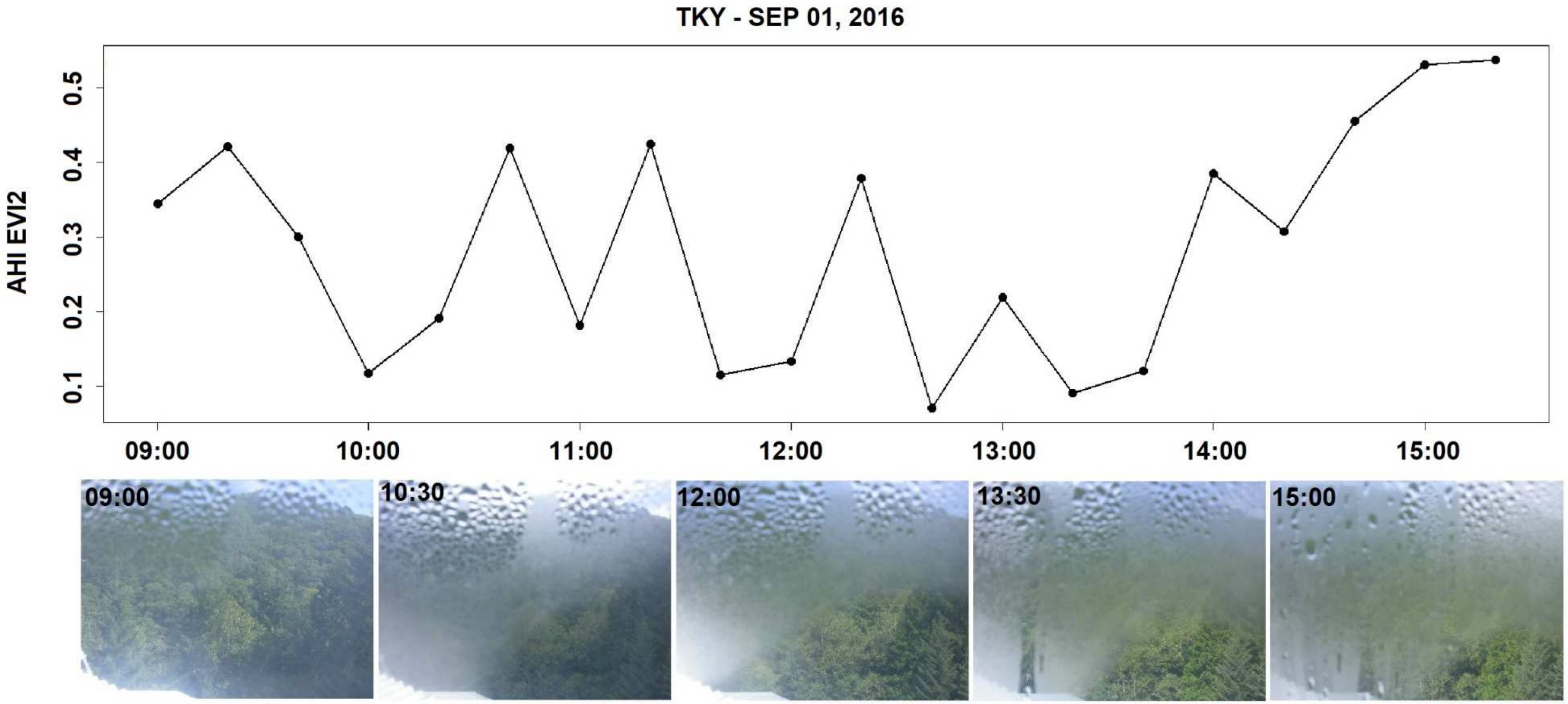


1147

1148 **Figure S5**. The 20min EVI2 (top row) and 90min photographs (bottom row) between 09:00 and 15:00 at the TKY site on September 01, 2016.

1149

1150

1151

1152

1153

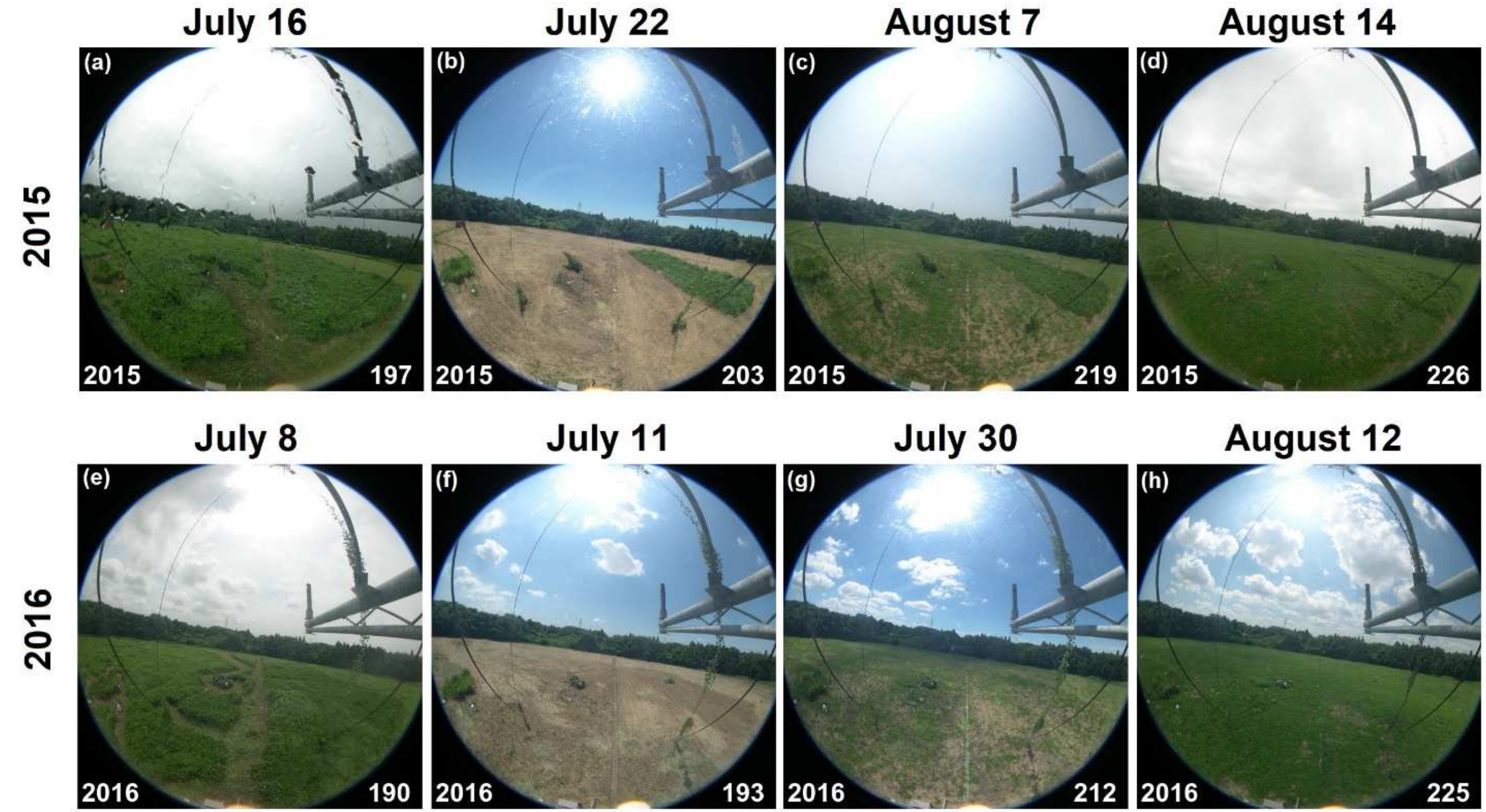


**Figure S6**. The rapid harvest and regrowth of grass during summer at the TGF site in 2015 and 2016. Day of year is reported at the lower right corner of each panel.